The CARMENES search for exoplanets around M dwarfs

Understanding the wavelength dependence of radial velocity measurements

S. V. Jeffers¹, J. R. Barnes², P. Schöfer³, S. Reffert⁴, V. J. S. Béjar^{5,6}, A. Quirrenbach⁴, A. Reiners⁷, Y. Shan^{7,8}, M. R. Zapatero Osorio⁹, B. Fuhrmeister¹⁰, P. J. Amado³, J. A. Caballero⁹, I. Ribas^{11,12}, C. Cardona Guillén^{5,6}, F. Del Sordo^{11,12}, M. Fernández³, A. García-López⁹ A. Guijarro¹³, A. P. Hatzes¹, M. Lafarga^{14,15}, N. Lodieu^{5,6}, M. Kürster¹⁶, K. Molaverdikhani¹⁷, D. Montes¹⁸, J. C. Morales^{11,12}

- ¹ Thüringer Landessternwarte Tautenburg, Sternwarte 5, D-07778 Tautenburg, Germany e-mail: sandrajeffers.astro@gmail.com
- ² School of Physical Sciences, The Open University, Walton Hall, MK7 6AA, Milton Keynes, United Kingdom
- ³ Instituto de Astrofísica de Andalucía (CSIC), Glorieta de la Astronomía s/n, E-18008 Granada, Spain
- ⁴ Landessternwarte, Zentrum für Astronomie der Universität Heidelberg, Königstuhl 12, D-69117 Heidelberg, Germany
- ⁵ Instituto de Astrofísica de Canarias, c/ Vía Láctea s/n, E-38205 La Laguna, Tenerife, Spain
- ⁶ Departamento de Astrofísica, Universidad de La Laguna, E-38206 Tenerife, Spain
- ⁷ Institut für Astrophysik and Geophysik, Georg-August-Universität, Friedrich-Hund-Platz 1, D-37077 Göttingen, Germany
- 8 Centre for Planetary Habitability, Department of Geosciences, University of Oslo, Sem Saelands vei 2b, 0315 Oslo, Norway
- ⁹ Centro de Astrobiología (CSIC-INTA), ESAC, Camino Bajo del Castillo s/n, E-28692 Villanueva de la Cañada, Madrid, Spain
- ¹⁰ Hamburger Sternwarte, Universität Hamburg, Gojenbergsweg 112, D-21029 Hamburg, Germany
- ¹¹ Institut de Ciències de l'Espai (CSIC), Campus UAB, c/ de Can Magrans s/n, E-08193 Bellaterra, Barcelona, Spain
- ¹² Institut d'Estudis Espacials de Catalunya, E-08034 Barcelona, Spain
- ¹³ Centro Astronómico Hispano en Andalucía (CAHA), Observatorio de Calar Alto, Sierra de los Filabres, E-04550 Gérgal, Almería, Spain
- ¹⁴ Department of Physics, University of Warwick, Gibbet Hill Road, Coventry CV4 7AL, UK
- ¹⁵ Centre for Exoplanets and Habitability, University of Warwick, Coventry CV4 7AL, UK
- ¹⁶ Max-Planck-Institut für Astronomie, Königstuhl 17, D-69117 Heidelberg, Germany
- ¹⁷ Fakultät für Physik, Universitäts-Sternwarte, Ludwig-Maximilians-Universität München, Scheinerstr. 1, D-81679 München, Germany
- ¹⁸ Facultad de Ciencias Físicas, Departamento de Física de la Tierra y Astrofísica & IPARCOS-UCM (Instituto de Física de Partículas y del Cosmos de la UCM), Universidad Complutense de Madrid, E-28040 Madrid, Spain

Received 20 July 2023 / Accepted 20 October 2024

ABSTRACT

Context. Current exoplanet surveys are focused on detecting small exoplanets orbiting in the liquid-water habitable zones of their host stars. Despite the recent significant advancements in instrumental developments, the current limitation in detecting these exoplanets is the intrinsic variability of the host star itself.

Aims. Our aim is to use the full CARMENES guaranteed time observations (GTO) data set spanning more than 8 years of observations of over 350 stars to investigate the wavelength dependence of high-precision radial velocities (RV), as stellar activity features should exhibit a wavelength dependence while the RV variation due to an orbiting planet will be wavelength independent.

Methods. We use the chromatic index (CRX) to quantify the slope of the measured RVs as a function of logarithmic wavelength. We investigate the dependence of the CRX in the full Carmenes GTO sample on 24 stellar activity indices in the visible and near-infrared channels of the CARMENES spectrograph and each star's stellar parameters. We also present an updated convective turnover time scaling for the calculation of the stellar Rossby number for M dwarfs.

Results. Our results show that approximately 17% of GTO stars show a strong or a moderate correlation between CRX and RV. We can improve the measured RVs by a factor of up to nearly 4 in rms by subtracting the RV predicted by the CRX-RV correlation from the measured RVs. Mid M dwarfs with moderate rotational velocities, moderate CRX-gradients and quasi-stable activity features have the best rms improvement factors.

Conclusions. We conclude that the CRX is a powerful diagnostic in mitigation of stellar activity and the search for low mass rocky planets.

Key words. stars: activity – stars: low-mass – stars: starspots – stars: magnetic field – techniques: radial velocities; planets – detection

1. Introduction

In recent years there has been exceptional progress in wavelength calibration and the development of high-precision,

highly-stable instrumentation with the aim of detecting small rocky exoplanets orbiting in the liquid-water habitable zones of their host stars using the RV technique. These include ESPRESSO (Pepe et al. 2021), EXPRES (Jurgenson et al. 2016)

and MAROON-X (Bean 2020) among others with tens of cm s⁻¹ precision. Recently, Suárez Mascareño et al. (2020) reported the achievement of a precision of 30 cm s⁻¹ for ESPRESSO observations of Proxima Centauri. The current limitation in detecting small rocky planets is not instrumental capability, but the intrinsic variability of the host stars themselves (see recent works such as Crass et al. 2021; Zhao et al. 2022, and references therein).

All stars with masses just above and lower than the Sun possess an internal convection zone and exhibit some degree of magnetic activity from very low (e.g. the early M dwarf GJ 887: Jeffers et al. 2020) to very high (e.g. the early and mid M dwarfs AU Mic and EV Lac: Cale et al. 2021; Klein et al. 2022; Jeffers et al. 2022; Bellotti et al. 2022). The presence of this activity induces an asymmetry in the shape of the stellar photospheric absorption lines which limits our ability to determine the star's centre-of-mass motion via the position of the line's centre (Dravins et al. 1981; Saar & Donahue 1997; Lagrange et al. 2010; Meunier et al. 2010; Reiners et al. 2010; Barnes et al. 2011; Dumusque et al. 2014; Haywood et al. 2014). This consequently results in an additional activity-induced RV contribution which impacts the detection and the measurement of the masses of small planets orbiting close to their host stars. There are also a large number of methods that have been developed to remove the activity-induced component to the RVs. However, the conclusion is, from the extensive testing of different activityremoval methods by Zhao et al. (2022), that no method succeeds in routinely achieving a reduction in the RV rms to sub-meterper-second levels.

In this work we aim to understand the wavelength dependent activity diagnostics of the full data set secured as part of the CARMENES GTO survey (Calar Alto high-Resolution search for M dwarfs with Exo-earths with Near-infrared and optical Échelle Spectrographs; Quirrenbach et al. (2018, 2020). The CARMENES GTO sample was selected to contain the brightest stars in the J band for each M dwarf sub-spectral type bin that are observable from Calar Alto Observatory in southern Spain and have no stellar companion within 5 arcsec. This selection procedure for the GTO sample ensures that it includes both magnetically active and inactive stars, and now after over 8 years of operation, and with more than 20 000 spectra in hand (Ribas et al. 2023), ensures that we have a statistically significant sample to understand the impact of stellar activity on high-precision RV measurements. One important diagnostic parameter in the search for exoplanets orbiting stars showing stellar activity is an analysis of the wavelength dependence of the measured RV values. This is because features of stellar activity such as dark cool starspots are typically wavelength-dependent because the contrast between starspots and the stellar photosphere is smaller at longer wavelengths. In contrast, the RV signal from an orbiting exoplanet is wavelength independent.

The chromatic index (CRX) is a measure of the RV variation as a function of wavelength. It is defined by taking the slope of the RVs in every spectral order as a function of logarithmic wavelength (Zechmeister et al. 2018). The CRX-index has been shown by Jeffers et al. (2022), using a low-resolution Doppler-imaging technique, to be directly correlated with starspot coverage for the mid M-dwarf EV Lac. This is consistent with (i) the simulations of Baroch et al. (2020), who combined the CRX-index with photometric observations of YZ CMi to constrain the spot-filling factor and YZ CMi's spot and photosphere temperature contrast, and (ii) the previous work of Tal-Or et al. (2018), who investigated the CRX-index for only the most active stars in the CARMENES GTO sample using the first 1.5 years of CARMENES data. More recently, Lafarga et al. (2020) inves-

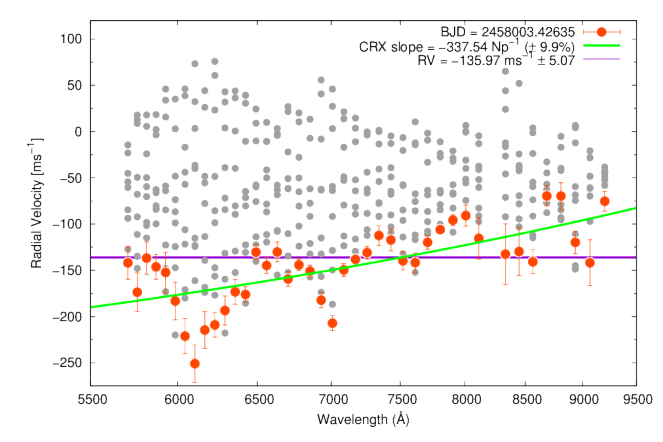


Fig. 1. Illustration of the RV variation with wavelength, where the central wavelength is given for each order. Shown are the same data as in Figure 2, with the steepest positive slope shown by red points. The green line indicates the slope of these points, which is the CRX-index for each individual spectrum. The weighted RV measurement is shown by the purple line. The wavelength spacing is logarithmic.

tigated periodicities found in RVs and nine activity indicators in the CARMENES GTO sample. They concluded that the CRX is as efficient as the line bisector (Queloz et al. 2001) as indicator of activity for active M dwarfs. Other recent work by Collier Cameron et al. (2021) (and also Lisogorskyi et al. 2019) has exploited the wavelength dependence of RV induced by stellar activity to separate RVs with dynamical origin from stellar activity induced variability.

In this paper we aim to empirically understand the wavelength variations of RVs using the CRX-index, and to quantify how to remove this contribution from the RVs. In Section 2 we define the CRX-index and in Section 3 we describe the observations and define how the CRX stars were selected from the full CARMENES GTO sample. Section 4 we investigate the dependence of CRX-index on fundamental stellar parameters. In Section 5, we use the wavelength information contained in the CRX-index to remove stellar activity from the RVs. We discuss the implications of our results in Section 6.

2. CRX: dependence of RVs with wavelength

2.1. Definition of the CRX

The CRX-index is defined as the slope of the RV as a function of logarithmic wavelength (Zechmeister et al. 2018) for each spectrum. The RV of each spectrum is computed using weighted averages to account for the wavelength dependence of the RVs (more details later in Section 3.1). This is illustrated in Figure 1, which shows the wavelength dependent RVs of 10 spectra of the mid-M dwarf EV Lac. The spectrum exhibiting the steepest positive gradient is illustrated with red points and a linear fit in green. The RV value computed by serval is shown as a horizontal purple line.

Figure 2 shows the CRX calculation in more detail for the same 10 spectra that are illustrated in Figure 1. Because the spectra span less than two complete rotations of EV Lac ($P_{\rm rot}=4.349$ d; Jeffers et al. 2022), the effects of evolution due to stellar activity should be minimal. Each spectrum is coloured according to the stellar rotation phase. The CRX-index measured for each of the spectra in Figure 2 (top left panel) is shown as a function of RV in Figure 2 (top right panel), where the colour coding is the same in both panels.

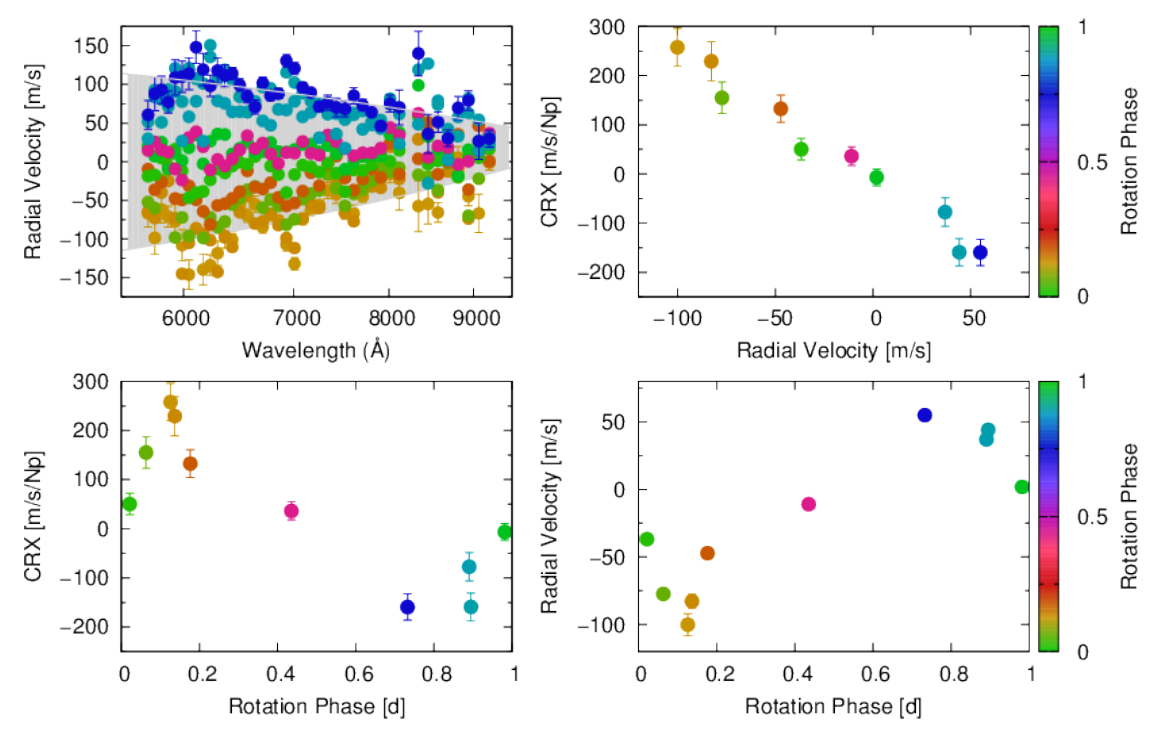


Fig. 2. Illustration of the behaviour of the CARMENES visible channel CRX for the mid-M dwarf EV Lac. Top Left: Variation of RV as a function of wavelength (spacing is logarithmic). The CRX-index is the slope of RV vs $log(\lambda)$ for each spectrum. A total of 10 CARMENES spectra are shown covering approximately one stellar rotation. The upper and lower boundaries are the fits to the most positive and negative RV values. Top right: The CRX-gradient, illustrating the CRX-index as a function of *mean* RV. Bottom Left and Bottom Right: CRX vs rotation phase and RV vs rotation phase illustrating the anti-correlation of CRX-index (i.e. the negative CRX-gradient shown in the top right panel). The plotted points in each panel are colour coded according to stellar rotation phase.

The gradient of the CRX-index versus RV distribution for a series of spectra is referred to as the CRX-gradient in the work that follows. For each star, we define the CRX-length as RV_{max} - RV_{min} , where the RV_{min} and the RV_{max} are the minimum and maximum RV values from all of the available spectra (using 90 and 10 percentiles). We prefer this definition since CRX variation (CRX_{max} - CRX_{min}) and CRX are directly related, while CRX-length is most readily calculated directly from the RVs, even in the absence of CRX-index measurements. The large variations in the CRX-index as a function of rotation phase (as illustrated in Figure 2) demonstrate how the CRX-index evolves over the stellar rotation period due to the presence of activity features on the stellar surface. The CRX-index for each individual spectrum, and consequently the CRX-gradient for a series of spectra, has been directly linked to the distribution of dark starspots on the stellar surface using low resolution Doppler imaging techniques by Jeffers et al. (2022). The lower two panels of Figure 2 show the variation of CRX-index and RV as a function of stellar rotational phase, with the same colouring as in the upper panels.

The data shown in Figure 2 are for the VIS channel only as the errors in the NIR channel are too high for meaningful interpretation for the case of EV Lac. Even though the NIR data are not shown, we do not expect to see a convergence of the slopes at longer wavelengths as is suggested by the outer edges of the light grey region in Figure 2 (top left panel). As discussed by Jeffers et al. (2022), a black-body scaling of the spot and photospheric flux ratios will remain constant continuing to NIR wavelengths, in agreement with PHOENIX models for the spot / photosphere ratio. A more detailed description of the full data set of EV Lac was previously presented by Jeffers et al. (2022).

2.2. Comparison of the CRX with different instruments

The CRX will show different behaviour when investigated with different spectrographs with varying wavelength coverage and spectral resolution. The comparison of the CRX between data secured with HARPS and CARMENES has been previously investigated by Zechmeister et al. (2018) for the stars YZ CMi, and GJ 3379, and Kossakowski et al. (2022) for AD Leo. In general the CRX shows a negative slope for both HARPS and CARMENES datasets of YZ CMi while for GJ 3379, only the CARMENES data show a significant chromatic variation. Similarly, CARMENES M dwarf K2-18 has been reported by Radica et al. (2022) to show chromatic behaviour at a level that is below our threshold of Pearson's r > 0.5. Similar to GJ 3379, this is not visible in the HARPS dataset of K2-18. Surprisingly, the CRX of AD Leo shows a positive slope for archival HARPS data and a negative slope for CARMENES data (Kossakowski et al. 2022; Zechmeister et al. 2018) and significantly lower amplitude for much redder wavelengths (Carmona et al. 2023). The comparison of chromaticity of RVs across a very broad wavelength regimes has the potential to give a crucial insight into the activity of these stars. However, simultaneous observations across a broad wavelength range are required to truly compare the wavelength dependence as features of stellar activity can evolve on timescales of a few stellar rotation periods.

2.3. Modelling the CRX

The effect of dark starspots on the wavelength dependence of RVs has previously been investigated by Desort et al. (2007); Barnes et al. (2011); Collier Cameron et al. (2021) among many others. In particular, the CRX has been simulated by Baroch

et al. (2020) using spectroscopic and photometric data for the mid-M dwarf YZ CMi. They demonstrated that the CRX-index, computed for each spectrum, can be used to determine, and break the degeneracy between, the spot-filling factor and temperature contrast between the starspot and unspotted photosphere.

Recent work has shown that the CRX-index versus RV relation can have an inclined lemniscate (∞) or figure-of-eight shape, with a typically negative slope, which results from a slight phase offset between the phase curves of the RVs and the CRX values (examples include Baroch et al. 2020; Jeffers et al. 2022, for YZ CMi and EV Lac respectively). This is comparable to the inclined-lemniscate shape established for RV versus Bisector Inverse Slope (BIS) relations for co-rotating cool spots (Desort et al. 2007; Saar & Donahue 1997; Boisse et al. 2011). For the BIS, Boisse et al. (2011) attribute this to result from foreshortening and limb-darkening effects, while for the CRX Baroch et al. (2020) consider that the offset results from the combined effects of limb darkening and convective blue shift. The example of the CRX-index versus RV relation shown Figure 2 for the mid-M dwarf EV Lac is almost a straight line due to the dominance of high-latitude spot features (see the surface brightness maps reconstructed by Jeffers et al. (2022)) and to the limited time sampling of the data which covers only a few rotation periods. We would expect a higher amplitude lemniscate shape if there was a higher degree of spot coverage located at equatorial latitudes as has been modelled for the BIS (Boisse et al. 2011).

2.3.1. Spot to photosphere contrast

The spot to photospheric temperature contrast decreases towards redder wavelengths because the contrast between dark starspot and the photosphere is smaller at longer wavelengths. As this is one of the key diagnostic parameters of the CRX, we first update the temperature contrast relation originally published by Berdyugina (2005) who only used contrasts derived from photometric data sets for spectral types earlier than M3V. Here, we additionally include values used in Doppler imaging studies covering the full spectral type range from early-G to late-M (Table 1), as well as the MHD simulations of starspots for different spectral types (Panja et al. 2020). Our revised spot to photosphere temperature contrast (using Doppler Imaging results only) is equated as follows:

$$\Delta T = a T_{\text{phot}} + b \tag{1}$$

where a = 0.47 and b = -926.97 K. The fit to all Doppler Imaging data is plotted in Figure 3.

2.3.2. CRX-gradient and length

The simulations of Baroch et al. (2020) show that the gradient of the CRX-RV relation is an important diagnostic as it provides a key insight into how quickly the RV variations induced by a cool starspot decrease as a function of increasing (logarithmic) wavelength. In the simulations of Baroch et al. (2020), the CRX-gradient primarily depends on the spot to photosphere temperature contrast ratio for the case of one large spot located at a latitude of 78°. In addition to the CRX-gradient, Baroch et al. (2020) also reported that the length of the CRX-index versus RV relation depends on both the spot-to-photosphere contrast and the spot filling factor. This is expected because for a given single spot size (i.e. a star with a fixed filling factor), the wavelength dependent RV amplitude and hence gradient measured by

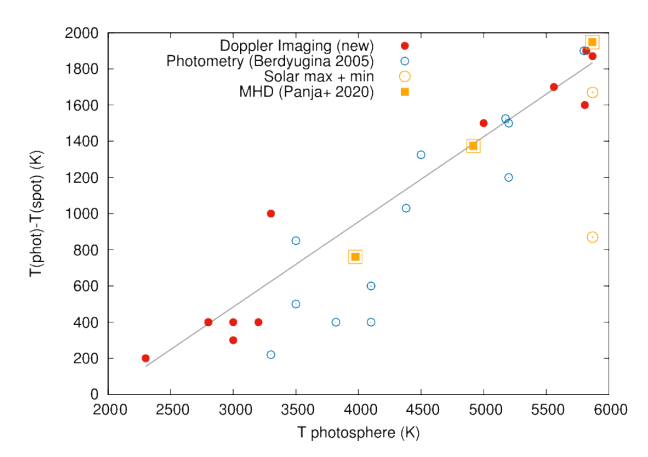


Fig. 3. Revised photospheric to spot temperature. Original photometric data points from Berdyugina (2005) are shown as light blue open circles. Doppler imaging values are shown as filled red circles where the values are taken from Table 1 and the values for the Sun are shown as two large open light blue circles with a temperature of 5800 K.

Table 1. Empirical data used to derive spot to photospheric temperature contrasts using the Doppler imaging technique.

| Star | Sp. | $T_{ m phot}$ | $T_{\rm spot}$ | ΔT | Ref. |
|-----------|--------|---------------|----------------|------------|------|
| | type | (K) | (K) | (K) | |
| HD 106506 | G1.0 V | 5870 | 4000 | 1870 | 1 |
| EK Dra | G1.5 V | 5561 | 3861 | 1700 | 2 |
| HD 171488 | G2.0 V | 5808 | 4200 | 1600 | 3 |
| HD 29615 | G3.0 V | 5820 | 3920 | 1900 | 4 |
| AB Dor | K0.0 V | 5000 | 3500 | 1500 | 5 |
| EV Lac | M3.5 V | 3300 | 2300 | 1000 | 7 |
| V394 Peg | M4.0 V | 3200 | 2800 | 400 | 8 |
| HU Del | M4.5 V | 3000 | 2700 | 300 | 9 |
| GJ 65A | M5.5 V | 2800 | 2400 | 400 | 10 |
| GJ 65B | M6.0 V | 2800 | 2400 | 400 | 10 |
| LP 944-20 | M9.5 V | 2300 | 2100 | 200 | 9 |

References. 1: Waite et al. 2017; 2: Waite et al. 2017; 3: Jeffers & Donati 2008; 4: Waite et al. 2015; 5: Jeffers 2005; 6: Jeffers et al. 2022; 7: Morin et al. 2008a; 8: Barnes et al. 2015a; 9: Barnes et al. 2017

CRX-index is larger for a larger spot-to-photosphere contrast. Similarly, for a fixed spot to photospheric contrast, increasing a spot's size, and thus the spot filling factor, will also lead to a greater CRX-length.

The models of Baroch et al. (2020) considered the impact of one starspot located at high latitudes on the surface of the mid-M dwarf YZ CMi. However results from Doppler imaging studies (examples are listed in Table 1) show that in reality, the surfaces of M dwarfs are likely to be much more densely spotted. In this work we use the CRX-gradient and the CRX-length as the two main diagnostic parameters of our investigation. We investigate how the CRX-gradient and CRX-length of stars in the CARMENES GTO sample depend on their fundamental stellar parameters and levels of stellar activity.

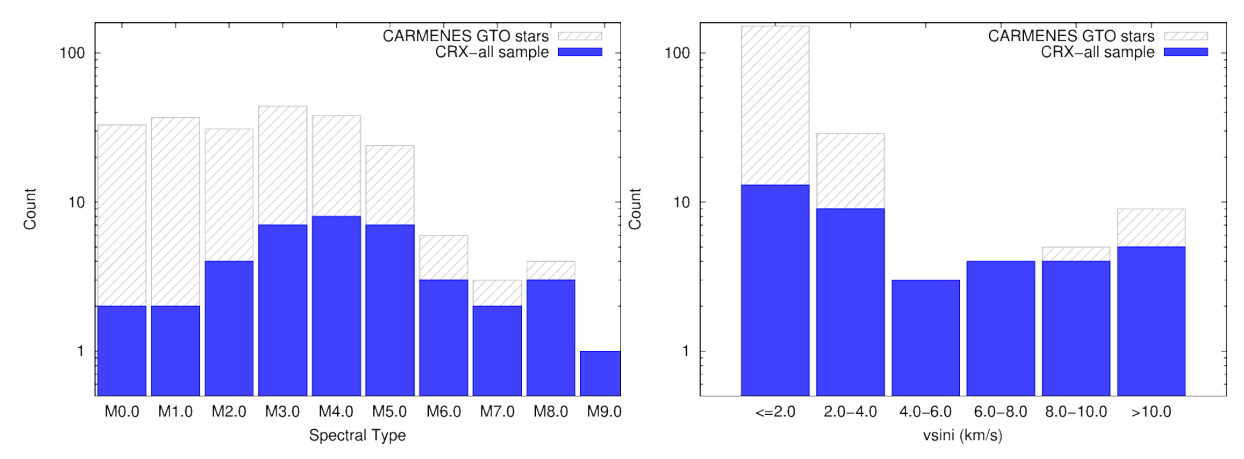


Fig. 4. Spectral type distribution (left panel) and the distribution of $v \sin i$ of the CRX-all sample, coloured in blue. Also shown are all of the CARMENES GTO stars with more than 25 observations as indicated by shaded grey bars.

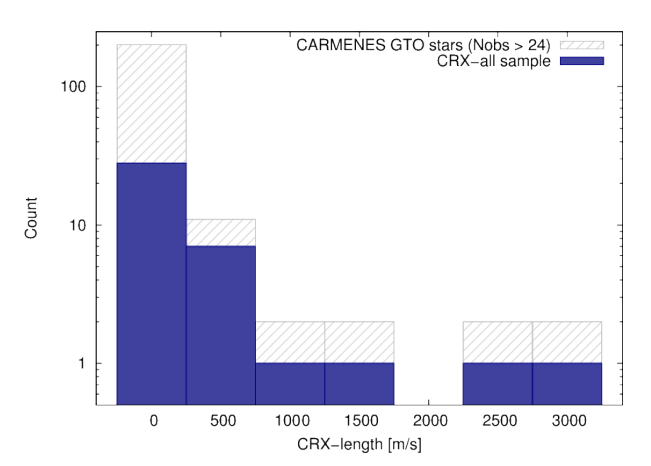


Fig. 5. Distribution of CRX-length for the CARMENES GTO sample (light grey) and the CRX-all sample (navy). For clarity, the CRX-length values of the CARMENES GTO sample are only shown up to a value of $3000~{\rm m\,s^{-1}}$

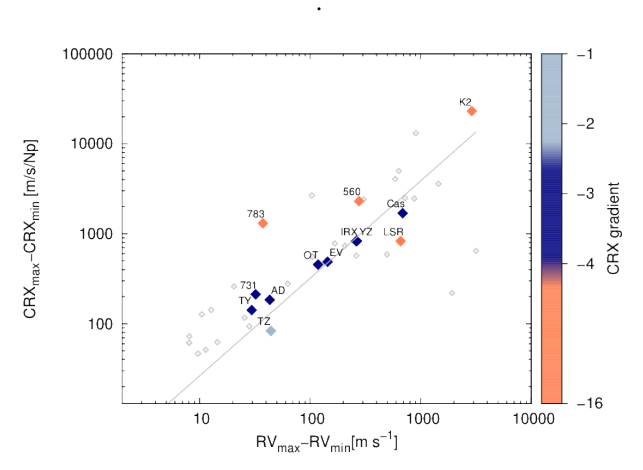


Fig. 6. The variation of CRX (CRX_{max} - CRX_{min}) as a function of RV variation (CRX-length = RV_{max} - RV_{min}). Fitted is a straight line to moderate slopes (coloured navy). Points are coloured by CRX-gradient.

3. Data

3.1. Observations and data processing

The data investigated in this work are the full set of CARMENES Guaranteed Time Observations (GTO) of more than 350 M dwarfs which have been observed since the start of the

CARMENES GTO survey in 2016. The CARMENES spectrograph is installed at the 3.5 m telescope at Calar Alto Observatory in Spain. It comprises two fibre-fed and cross-dispersed spectrographs, one at visible wavelengths (VIS, 520–960 nm) and the other at near-infrared wavelengths (NIR, 960–1710 nm) with a resolution of \sim 94 600 in the VIS and \sim 80 400 in NIR and an average sampling of 2.8 pixels (Quirrenbach et al. 2018). The data were processed in the usual manner for CARMENES data, i.e. with caracal (CARMENES reduction and calibration software; Zechmeister et al. 2014; Caballero et al. 2016), and the RVs were calculated using serval (Spectrum radial velocity analyzer Zechmeister et al. 2018) using weighted averages to account for the wavelength dependence of the RVs, where the individual orders are weighted. The impact of telluric lines on the measured RVs was removed (Nagel et al. 2023) using the template division telluric modeling technique. The nightly-zeropoint (NZPs) were also subtracted from the serval RV measurements (see Ribas et al. (2023) section 4.4 for a detailed explanation).

3.2. CARMENES NIR channel

In this work we only use data from the CARMENES VIS channel and not from the CARMENES NIR channel because the NIR channel yields RV measurements of less precision than the VIS channel. This is partly because of the diminished RV information content in the observed NIR domain Reiners et al. (2018). But also, the CARMENES NIR channel suffered from thermo-mechanical instability since the start of operations and until some corrective measures were applied a few years later. Consequently, the NIR RV data were in general not used during the exploitation of Guaranteed Time Observations (but see Morales et al. (2019) and Bauer et al. (2020)). Subsequent instrument upgrades have dramatically improved the precision of the NIR channel (Schaefer et al. 2024; Varas et al. 2024, in prep) and a careful analysis of the newly collected NIR data is undergoing

3.3. Activity Indices and CCF parameters

Given the large wavelength coverage of CARMENES we have a large number of activity indicators available. We use a total of 26 indicators as follows

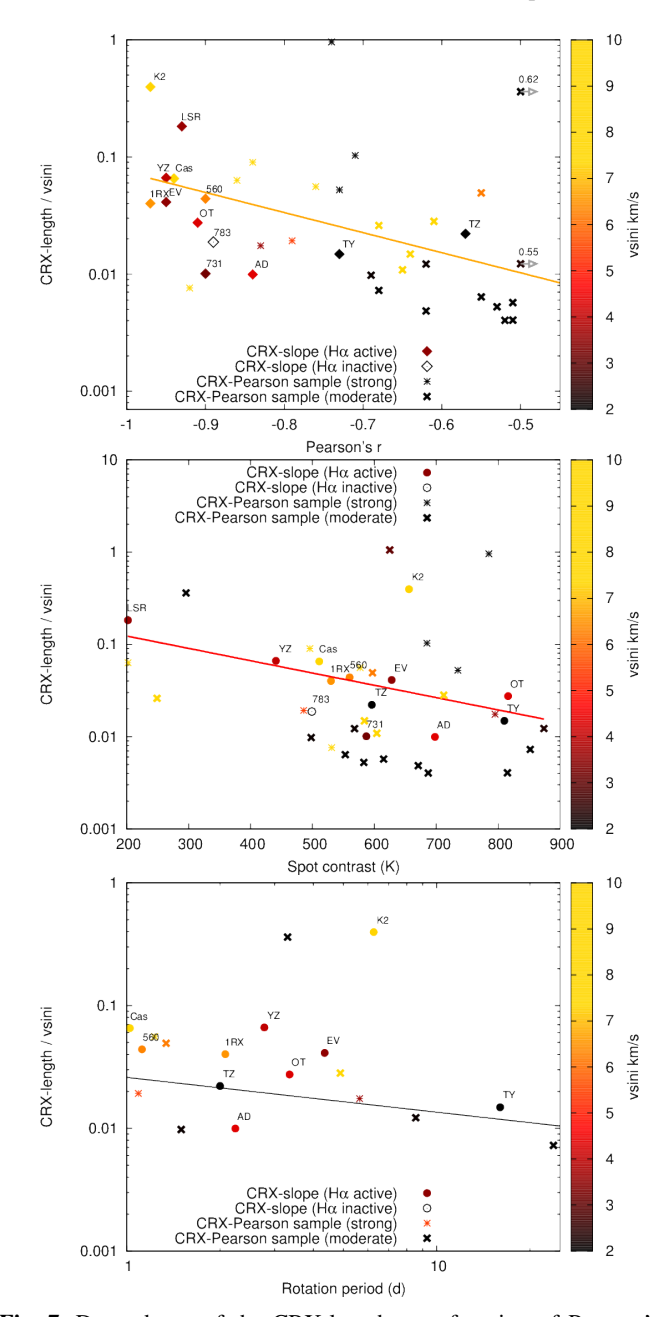


Fig. 7. Dependence of the CRX-length as a function of Pearson's r value (upper panel) and spot contrast (middle panel) and rotation period (lower panel) for the CRX-all stars sample. Closed symbols indicate $H\alpha$ active stars and open symbols $H\alpha$ inactive stars. Points are coloured by projected stellar rotational velocity ($v \sin i$). The CRX-slope stars are labelled as indicated in Table A.1. In the top panel, the two arrows indicate two stars with positive Pearson's r correlation. Their true Pearson's value is shown in the label for each point.

- Six RV, CRX and differential line widths (dLW) calculated by serval i.e. RV_{VIS} and $RV_{NIR},\ CRX_{VIS}$ and $CRX_{NIR},\ dLW_{VIS}$ and $dLW_{NIR}.$
- Sixteen activity indices at VIS and NIR wavelengths computed following the procedure described by Schöfer et al. (2019). The full list of spectral line indices comprise: $\log(L_{\rm H\alpha}/L_{\rm bol})$, pEW(H α), HeD3, NaD, Ca IRT-a,b,-c, He I 10830, Pa β , CaH2, CaH3, TiO 7050, TiO 8430, TiO 8860, VO 7436, VO 7942, and FeH Wing-Ford. We define stars with positive pEW(H α), where H α is in absorption, to be H α inactive stars and with negative values, where

- ${\rm H}\alpha$ is in emission, to be ${\rm H}\alpha$ active stars. The minimum detectable emission in the ${\rm H}\alpha$ line depends on the resolution of the spectrograph and the signal-to-noise of the data and has been shown by Schöfer et al. (2019) to be $-0.3\,{\rm \AA}$ for CARMENES.
- Four cross correlation function (CCF) parameters, CCF-Contrast, CCF-RV, CCF-FWHM, and CCF-BIS were computed following Lafarga et al. (2020).

3.4. CRX-all sample

From the full CAMRENES GTO sample of 350 stars, firstly, we select stars with a minimum number of observations $N_{\rm obs} > 25$ as this is the minimum number of observations required to give a reliable CRX-index versus RV relation, and to provide a statistically significant correlation with activity indicators. The CARMENES GTO sample with $N_{\rm obs} > 25$ comprises a total of 215 stars and is referred to as CARMENES $N_{\rm GTO}25$ sample in the rest of this work. Parameters for all 215 CARMENES $N_{\rm GTO}25$ stars are listed in Table B.1 (Appendix).

We then computed the statistical significance of the correlation of CRX-index with RV for each of the 215 stars using Pearson's r coefficient. We define a strong correlation (or anticorrelation) where Pearson's r>|0.7|, and a moderate correlation to be 0.5<|r|<0.7. The statistical significance is computed by the Student's t-test probability value, p. We assumed values of p<0.03 imply no strong evidence to reject the (no correlation) null hypothesis. There are a total of 39 stars with a strong or a moderate correlation and these stars are referred to as CRX-all in the work that follows and are listed in Table A.1. From this, 21 stars have strong correlations between the CRX-index and RV and 18 stars have a moderate correlation.

3.5. CRX-slope sample

The CRX-all sample is further classified based on a visual inspection of the CRX-index versus RV relation for each star. A total of 13 stars exhibit a tight linear CRX-index versus RV relationship and comprise both strong and moderate statistical CRX-index versus RV correlations. This sample is referred to as the CRX-slope sample in the rest of this work. To avoid confusion we refer to the actual measured value of the CRX slope as the CRX-gradient in the rest of this work. The CRX-index versus RV relation is shown for each of these stars in Figure A.1.

3.6. CRX-Pearson sample

The 26 remaining stars are refereed to as the CRX-Pearson sample in the rest of this work and are subdivided into Pearson-strong sample comprising 9 stars and Pearson-moderate sample comprising 17 stars. The CRX-index versus RV for these two samples are respectively shown in Figures A.2 and A.3. The RV-CRX correlation deviates from a straight line in this sample, where the deviations can take the form of a high degree of scatter or a generally extended cloud shape. The reasons for these deviations are not well understood and are beyond the current scope of this work.

Sample Summary:

- CRX-all: 39 stars with Pearson's strong, $|r| \ge 0.7$ (21 stars), or moderate, 0.5 < |r| < 0.7 (18 stars) correlations

- CRX-slope: 13 stars with a tight linear relationship, as in-
- spected visually; they are a subset of the the CRX-all sample CRX-Pearson: 26 stars with non-linear but moderate (17 stars) or strong (9 stars) Pearson's r values

3.7. Comparison to the CARMENES $N_{\rm GTO}$ 25-sample

The distribution of the CRX-all stars compared to the CARMENES $N_{\rm GTO}25$ -sample in terms of spectral type and projected stellar rotational velocity, or $v \sin i$ is shown in Figure 4. The 39 stars in the CRX-all sample cover all spectral types and broadly follows the spectral type distribution of the CARMENES $N_{\text{GTO}}25$ -sample. The distribution of $v \sin i$ values for the CRX-all stars and the CARMENES $N_{\rm GTO}25$ -sample are shown in Figure 4 (right panel). Approximately one third of the CRX-all stars have $v \sin i$ values $< 2.0 \,\mathrm{km \, s^{-1}}$, one third have $v \sin i$ values between 2.0–4.0 km s⁻¹ and the remaining third have values $4.0-10.5 \text{ km s}^{-1}$. The wavelength dependence of the RVs depends on many fundamental stellar parameters and in the following sections we will investigate the correlations and trends in the activity indices available from the CARMENES spectra.

4. Results: CRX: gradient and length

As previously discussed, preliminary models indicate that the two most useful parameters to characterise the CRX-index versus RV relation are its gradient and length. For the CRX-slope sample, the measured CRX-gradient values typically have slopes ranging from -2.65 Np^{-1} to -3.70 Np^{-1} (8 stars), with 4 stars having slopes in the range -4.6 Np^{-1} to -17 Np^{-1} , and 1 star having a very shallow slope of -1.16 Np^{-1} . The colouring of points in Figure 6 and subsequent Figures is chosen to reflect these broad groupings. We caution the direct interpretation of the steepest slopes for the 3 stars with the latest M-dwarf spectral types as for these stars there is less flux in the bluer orders and may potentially bias the results. Since our aim is to apply uniform analysis to all stars we have included these stars but do not draw any conclusions from them. In contrast, the steep slope of the young M 3.0 dwarf K2-33 results from very high levels of stellar activity given its young age.

CRX-length values range from 30 ms⁻¹ also for the M 2.5 dwarf TYC 3529-1437-1 to 2897 ms⁻¹ for the M 3.0 dwarf K2-33. The distribution of CRX-length values for the CRX-all sample compared to the CARMENES GTO sample is shown in Figure 5. In the work that follows we normalise the CRX-length by dividing the measured length by the stellar $v \sin i$.

Furthermore, in Figure 6 we show the CRX variation, CRX_{max} – CRX_{min}, as a function of the total RV variation, RV_{max} - RV_{min}, which we define as the CRX-length. The CRX-slope stars with moderate gradients show a linear increase with increasing RV variation.

Figure 7 illustrates the correlation between the CRX-length and the Pearson's r value where longer CRX-length / v sin i values have a higher Pearson's r value indicating a stronger statistical correlation. We note that low CRX-length values occur at low $v \sin i$ values. There was no correlation noted between the CRX-gradient and the Pearson's r value. We further investigated the correlation of CRX-gradient with the CRX-length. We find no correlation between these two parameters (plots not shown). We also examined the dependence of the CRX-gradient on the inferred spot to photospheric temperature contrast (see Section 2.2.1). While the results do not show a correlation with CRX-gradient, the CRX-slope stars lower contrasts for stars with higher CRX-length $/v \sin i$ values as shown in the middle panel of Figure 7. Stars with low $v \sin i$ values show the lowest CRXlength $/v\sin i$ values over a range of medium to high contrasts. Increasing the $v \sin i$ value for a given contrast often results in a higher CRX-length / $v \sin i$ value. The lower panel of Figure 7 shows that there is a tendency of stars with short stellar rotation periods to show slightly higher CRX-length $/v \sin i$ values.

Our initial results indicate that the interpretation and understanding the nature of the CRX is more challenging than suggested by the models (Baroch et al. 2020). However, it should be noted that only one starspot was modelled on the surface of YZ CMi and the reality is certainly more complicated. M dwarfs in general are likely to have more complicated distributions of starspots, where the latitude of the starspot will also have an impact on the CRX-gradient and length (Barnes et al. 2011), as well as plage regions (Meunier et al. 2010; Jeffers et al. 2014). Given that M dwarfs typically have much lower levels of convective blueshift compared to the more massive G and K dwarfs, its impact on the RV precision is unlikely to be a large effect (Liebing et al. 2021) compared to more massive solar-type stars. The dependence of the CRX gradient and length as a function of stellar activity parameters will be investigated in later sections of this work.

4.1. Dependence on activity indicators

In this section we investigate how the CRX gradient and CRXlength of each of the 13 CRX-slope stars depend on their measured activity indices in relation to the CRX-Pearson and CARMENES $N_{\text{GTO}}25$ -samples. The general patterns of activity in the CARMENES GTO sample have previously been presented and discussed in detail by Jeffers et al. (2018).

In the following Figures 8 to 13, the stars in the CRX-slope sample are shown as diamond symbols, CRX-Pearson strong stars with an asterisk symbol, CRX-Pearson moderate stars as a cross, and the remaining stars in the CARMENES $N_{\rm GTO}25$ sample are shown as small grey circular points. For each figure, the left and right panels are colour-coded based on the CRX gradient and the CRX-length $/v \sin i$, respectively.

The colouring for the CRX gradient and the CRX-length plots were chosen to represent the sample in terms of global groups rather specific stars. In the text that follows we discuss these plots in terms of the shallowest to the steepest slopes, and the shortest to the longest CRX-length values. The stellar activity indices that we investigate are stellar (i) rotational velocity or $v \sin i$ (Figure 8) (ii) chromospheric emission via H α (Figure 9), (iii) diagnostic of spot coverage via TiO7050 Å band (Figure 11). and finally (iv) average magnetic field strength (Figure 13).

4.2. CRX-gradient

In Table 2 we have summarised the information contained in the left-hand panels of Figures 8 to 13 to understand how the CRX gradient varies as a function of a range of stellar activity parameters. Comparing the gradients of the CRX-slope sample with the full CARMENES $N_{\rm GTO}$ 25-sample (see Jeffers et al. 2018), we conclude that the stars with the shallowest CRX-gradients are among the least active stars. Since there is only one star in this category we do not include the shallowest slopes in Table 2. Stars with moderate CRX gradients occur at early to mid-M spectral types, have high levels of stellar activity (Figures 8, 9) and show saturated $\log(L_{
m Hlpha}/L_{
m bol})$ and average magnetic field strengths (Figures 10, 13). Similarly, the steepest slopes occur

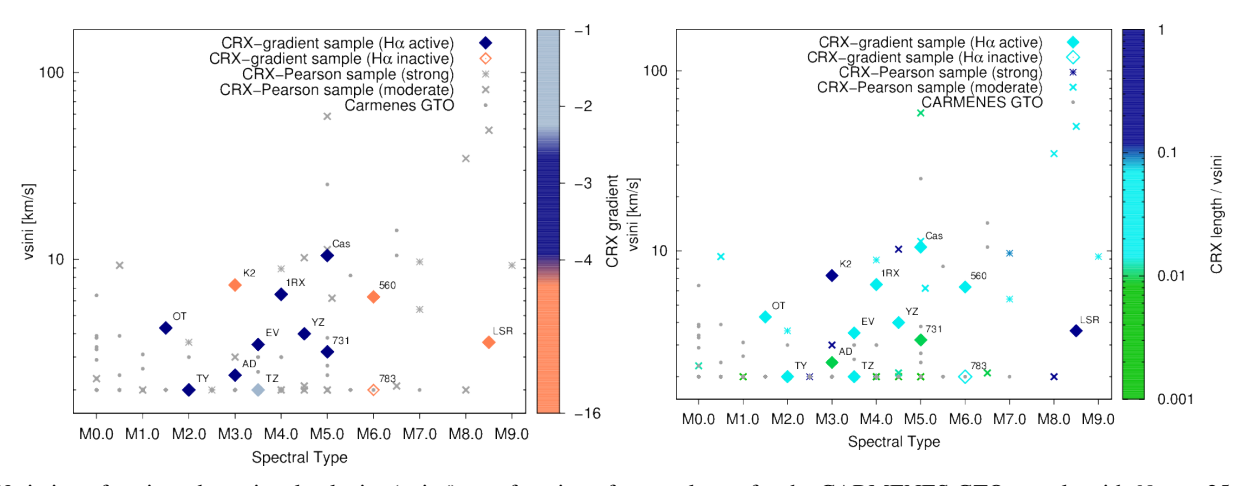


Fig. 8. Variation of projected rotational velocity ($v \sin i$) as a function of spectral type for the CARMENES GTO sample with $N_{\rm obs} > 25$. Stars in the CRX-slope sample are coloured according to the measured gradient(left panel) and CRX-length (right panel). Stars in the CRX-slope sample that are Hα active are indicated by closed symbols and Hα inactive stars as open symbols. The minimum $v \sin i$ value plotted is 2 km s^{-1} . The stars are labelled as indicated in Table A.1 and also whether their large-scale magnetic field geometry is SS: Stable + Strong or CW: Complex Weak.

Table 2. CRX-gradient with activity.

| Parameter | Moderate gradients | Steep gradients | Figure No |
|---------------------------------|--------------------------------------|-------------------|------------|
| Spectral Type | early to mid M | late-M | 8 |
| $v \sin i$ | $\leq 11 \mathrm{km}\mathrm{s}^{-1}$ | low to moderate | 8 |
| $\log(L_{ m Hlpha}/L_{ m bol})$ | active (high) | active (moderate) | 9 |
| $H\alpha$ sat / unsat | saturated | saturated | 10 |
| TiO 7050 | lowest value per SpT bin | late M hook | 11 |
| $\log(L_{\rm x}/L_{\rm bol})$ | saturated | ••• | not shown1 |
| Ave mag. field | highest | moderate | 13 |
| Ave mag. field sat / unsat | saturated | saturated | 13 |

Notes. The shallow gradients are not shown as this group only comprises only 1 star. (1) The $log(L_x/L_{bol})$ plot is not shown as many of the stars in the CRX-all sample do not have X-ray values.

Table 3. CRX-length with activity

| Parameter | arameter Shortest lengths | | Longest lengths | Figure |
|---------------------------------|--------------------------------|--------------------------|--------------------------|------------|
| Spectral Type | mid M | early to mid M | mid to late M | 8 |
| $v \sin i$ | $\leq 2-3.5 \text{ km s}^{-1}$ | moderate to high | moderate | 8 |
| $\log(L_{ m Hlpha}/L_{ m bol})$ | active: low to moderate | active: moderate to high | active: moderate to high | 9 |
| $H\alpha$ sat / unsat | unsaturated | both | saturated | 10 |
| TiO 7050 | lowest value per SpT bin lo | | late M hook + | 11 |
| $\log(L_{\rm x}/L_{\rm bol})$ | | saturated | saturated | not shown1 |
| Ave mag. field | moderate | highest | | 13 |
| Ave mag. field sat / unsat | unsaturated | both | | |

Notes. (1) The $\log(L_x/L_{bol})$ plot is not shown as many of the stars in the CRX-all sample did not have X-ray values.

at later M spectral types at moderate levels of activity (e.g. $v \sin i$ and $\log(L_{\rm H\alpha}/L_{\rm bol})$, Figures 8, 9). These stars show saturation at lower $\log(L_{\rm H\alpha}/L_{\rm bol})$ values compared to stars with mid-M spectral types (Mohanty & Basri 2003) (Figures 10, 13).

4.3. CRX-length

The correlations of the CRX-length / $v \sin i$ with the stellar activity indicators as shown in the right-hand panels of Figures 8 to 13 are summarised in Table 3 for ease of comparison. Generally, the shortest CRX-lengths are found for stars with low to mod-

erate ${\rm H}\alpha$ activity levels, with early to mid-M spectral types and moderate average magnetic field strengths (Figures 8, 9, 13). The moderate CRX-length values occur for very active stars and the longest lengths are for very active stars at late M spectral types. As noted in for the CRX gradient, activity in the latest M dwarfs saturates at lower $\log(L_{{\rm H}\alpha}/L_{\rm bol})$ values compared to mid M dwarfs (Figures 10, 13).

4.4. CRX-Pearson

The remaining stars in the CRX-Pearson sample follow the same trends. Stars with a strong Peason's correlation typically have longer lengths and are located at mid to late M spectral types. The correlation of the CRX-length with various parameters was previously discussed in more detail in Section 3.

4.5. Noteworthy points

Our aim has been to present the results of the CRX-gradient and length in the context of stellar activity in a clear and concise manner. In addition to the points already discussed, there are a few additional noteworthy points

- <u>Ca π H&K:</u> We also investigated the dependence of the CRX on the Ca π H&K lines as derived for the CARMENES GTO sample by Perdelwitz et al. (2021). However, there were only a few measurements available for the stars in the CRX-all sample from archival observations and it was not possible to determine any distinct correlations or trends; therefore these plots are not shown.
- X-ray: As summarised in Tables 2, and 3, X-ray data were only available for a small number of stars and it was not possible to derive any trends or correlations. As part of determining the $\log(L_x/L_{bol})$ relation as a function of Rossby number, we noticed that the fit parameters provided by Wright et al. (2018) in their equations 5 and 6 contain typos and are not the values derived from fitting the data in their Table 3. Notably, Reiners et al. (2022) independently found that there was an offset with the $\log \tau$ values from Wright et al. (2018) for very low mass stars. The correct scaling for the empirical calibration data of Wright et al. (2018) is as follows (and is an update to their Equations 5 and 6):

$$\log \tau = (0.58 \pm 0.04) + (0.28 \pm 0.01)(V - Ks) \tag{2}$$

$$\log \tau = (2.30 \pm 0.06) - (1.38 \pm 0.245)(M/M_{\odot}) + (0.22 \pm 0.19)(M/M_{\odot})^{2}$$
(3)

where $\log \tau$ is the convective turnover time and (V - Ks) is the magnitude difference between the V and Ks bands. The difference in the Rossby numbers derived using the fit parameters directly taken from Wright et al. (2018) and Equation 2 is illustrated in Figure 12 for the CARMENES GTO sample.

4.6. Stars not showing CRX-gradient

To understand why some stars show a clear CRX slope, or have a statistically significant correlation between CRX and RV, and other stars not, we inspected the CRX-index versus RV relations of seven stars that are not part of the CRX-all sample. These stars

were selected from regions that did not contain any stars from the CRX-all sample in (i) the $v\sin i$ versus spectral type and (ii) the $H\alpha$ versus spectral type plots. The stars are listed in Table 4 and their CRX-index versus RV relations are shown in Appendix A.4. The two stars, Teegarden's star and K2-18 are exoplanet hosts (Zechmeister et al. 2019; Sarkis et al. 2018; Plavchan et al. 2020; Martioli et al. 2021; Wittrock et al. 2022; Dreizler et al. 2024). For both Teegarden's star and K2-18, the planet-induced RV amplitude is a large fraction of the CRX-length value. In particular, K2-18 has been reported by Radica et al. (2022) to exhibit a wavelength dependence in RV based on the line-by-line method, but this below the Pearson's r threshold of 0.5 that we consider in this work.

5. Results: Removing stellar activity from RVs using CRX

The RV signatures resulting from presence of stellar activity such as spots and plage regions is wavelength dependent, due to the decrease of the photospheric / spot contrast, whereas a planetary companion would induce a RV signal that is wavelength independent. In this section we use the wavelength dependent information parameterised by the CRX to remove the signatures of stellar activity from the CRX-all sample of 39 stars. The subtraction of the CRX, via a linear fit to the CRX-RV anti-correlation, from the RV results in a decrease in the RV rms by a factor of up to 3.89 in the case of 1RXS J050156.7+4233 (labeled: 1RX). The results for the CRX-all sample are listed in Table A.1. We find a total of 9 stars or 25% of the CRX-all sample have a factor of improvement greater than 2.0.

There is a strong dependence of the factor of improvement (FoI) with Pearson's r value as shown in the top left-hand panel of Figure 14. A linear fit shows that this relation can be equated as follows:

FoI =
$$-18.51r - 14.48$$
 $(r < -0.80)$
FoI = $-1.98r + 0.04$ $(r > -0.80)$

where FoI is the factor of improvement and r is the Pearson's r value. Only 3 stars show an RV rms reduction that is greater than a factor of 3. These are 1RXS J050156.7+010845, YZ CMi and EV Lac, which will be referred to as the RV_{corr}3 stars in the rest of this work. All three stars have mid-M spectral types and are located on the saturated part of the rotation-activity correlation (Figure 10). For mid-M spectral types, this occurs at higher normalised H α values than for the latest M dwarf spectral types.

The correlation of the Factor of Improvement with stellar rotation period is shown in Figure 14 (upper right panel). The highest Factor of Improvement values are shown for fast to moderately rotating stars with rotation periods of approximately a few days to just less than 10 days. This is likely because such moderately rotating stars have more stable spot patterns.

The TiO indicator can be considered as an indicator of dark starspot coverage, even on slowly rotating and less active stars Vogt (1979); Amado & Zboril (2002); O'Neal et al. (2004). To remove the spectral type dependence that we previously showed in Figure 11, we plot the maximum minus the minimum value for each star (Figure 14 middle left panel). The RV_{corr}3stars show moderate values, while the cluster of low $v \sin i$ stars with very small Factor of Improvement values show very small TiO 7050 variations.

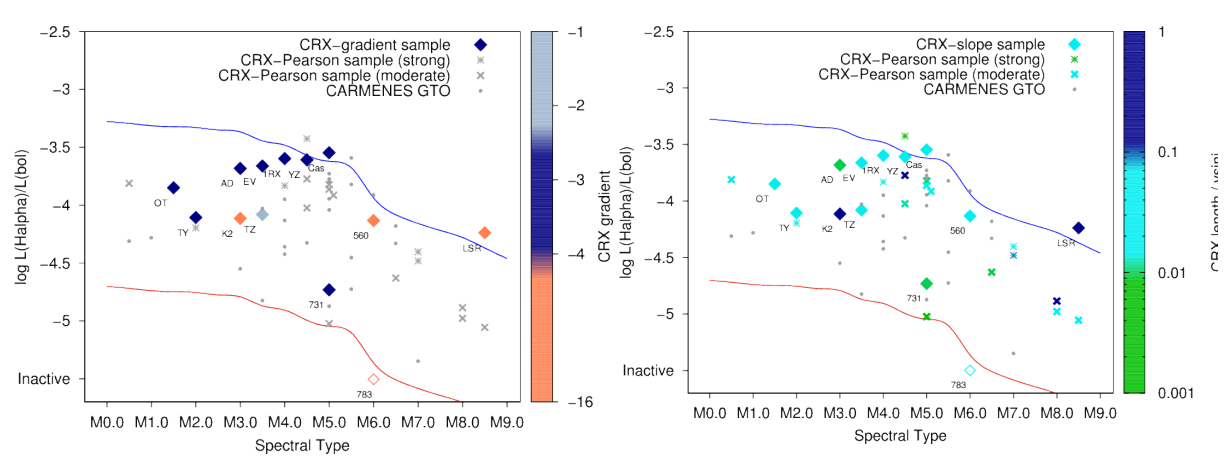


Fig. 9. Normalised Hα luminosities as a function of spectral type for CARMENES GTO sample with $N_{\rm obs} > 25$. The solid orange line indicates the minimum values of emission in the Hα line that our CARMENES observations can detect, which is defined to be pEW (Hα) = -0.3 Å (Schöfer et al. 2019). A population of extremely active stars with pEW(Hα) < -8.0 are indicated by the solid blue line as previously noted by Jeffers et al. (2018). Hα inactive stars are shown at the base of each plot as indicated by the y-axis. The stars in the CRX-slope sample are indicated by the diamond shapes which are coloured based on the CRX gradient of the data points in the left panel and CRX-length in the right panel. The stars are labelled as indicated in Table A.1.

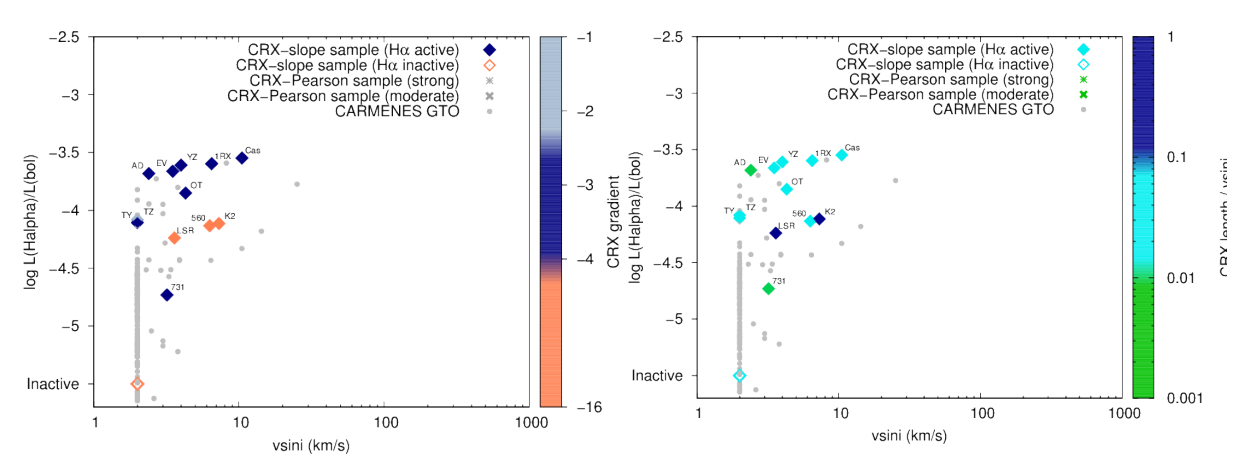


Fig. 10. Normalised H α luminosities as a function of projected rotational velocities $(v \sin i)$ for CARMENES GTO sample with $N_{\rm obs} > 25$. Stars in the CRX-slope sample are shown by diamond shaped point which are open for H α inactive stars and filled for H α active stars. The CRX-slope sample stars are coloured based on CRX-gradient (left panel) and CRX-length (right panel). The stars are labelled as indicated in Table A.1.

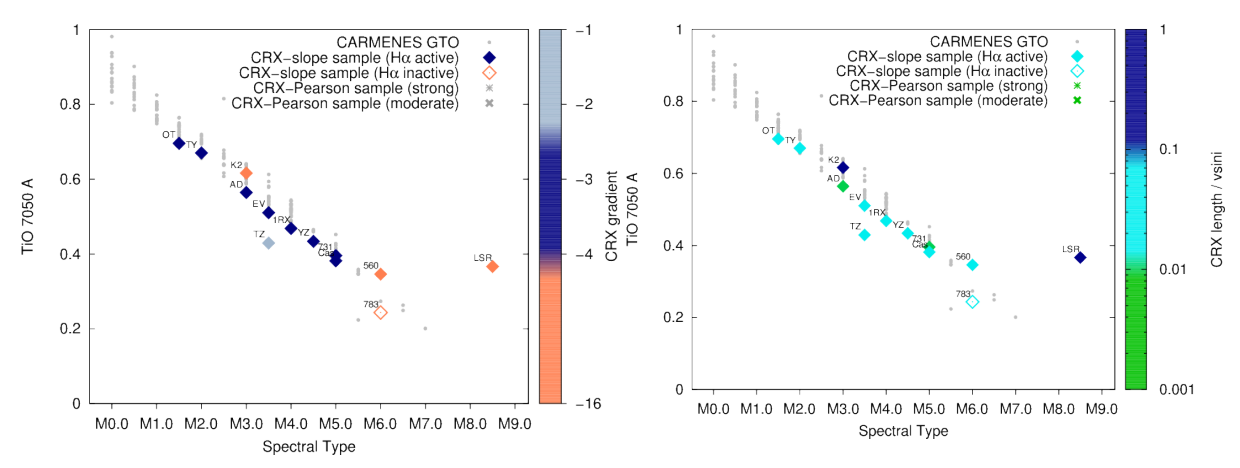


Fig. 11. Variation of TiO 7050 index as a function of stellar spectral type for the CARMENES GTO sample with $N_{\rm obs} > 25$. The CRX-slope sample of stars is indicated by diamonds which are filled for H α active stars and open for H α inactive stars. The CRX-slope sample stars are coloured depending on CRX-gradient (left panel) and CRX-length (right panel). The stars are labelled as indicated in Table A.1.

Table 4. Sample of stars not showing a CRX slope.

| Karmn | Name | Sp. | $v \sin i$ | $P_{\rm rot}$ | $\log L_{ m Hlpha}/L_{ m bol}$ |
|------------|-------------------------|--------|--------------------------------|---------------|--------------------------------|
| | | type | $(\mathrm{km}\mathrm{s}^{-1})$ | (d) | |
| J02530+168 | Teegarden's Star | M7.0 V | <2.0 | 96.00 | -5.40 |
| J05084-210 | 2MASS J05082729-2101444 | M5.0 V | 25.2 | 0.28 | -3.28 |
| J06024+498 | G 192-015 | M5.0 V | < 2.0 | 105.00 | Inact. |
| J07361-031 | BD-02 2198 | M1.0 V | 3.1 | 12.2 | -4.28 |
| J11302+076 | K2-18 | M2.5 V | < 2.0 | 38.83 | Inact. |
| J14257+236 | BD+24 2733 | M0.5 V | < 2.0 | 17.60 | Inact. |
| J19346+045 | BD+04 4157 | M0.0 V | 3.9 | 12.90 | Inact. |

References. The full list of stellar parameters for each of these stars is listed in the Appendix Table B.1. The rotation period of Teegarden's star is taken from Dreizler et al. (2024). CRX-RV relations for each of these stars are plotted in Figure A.4.

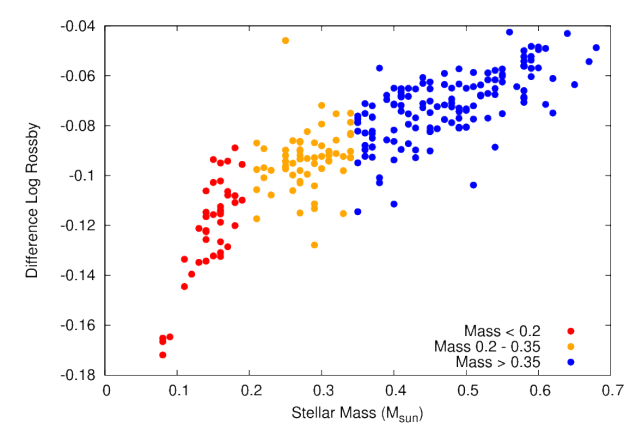


Fig. 12. Difference in Rossby number as a function of stellar mass derived using the fit in Equation 2 and the parameters published in Wright et al. (2018) (their equations 5 and 6). Points are coloured by stellar mass following Shan et al. (2024).

Furthermore, we show the factor of improvement as a function of normalised $H\alpha$ in Figure 14 (middle row right panel). Notably, the RV_{corr}3 stars have very high levels of $H\alpha$ activity. The remaining stars show $H\alpha$ values spanning the full range from low to high levels of $H\alpha$ activity.

Finally in the lower panels of Figure 14 we investigate the dependence of the Factor of Improvement value on the CRX-length / $v \sin i$ and spot contrast ratio (left and right panels respectively). The factor of improvement increases with increasing CRX-length / $v \sin i$ values, though importantly the RV_{corr}3 stars don't follow this trend with the highest factor of improvement values and moderate CRX-length / $v \sin i$ values. The lowest $v \sin i$ stars have the lowest factor of improvement values and the lowest CRX-length / $v \sin i$ measurements. The variation of the factor of improvement with spot contrast ratio shows a general trend of increasing factor of improvement values with decreasing spot contrast ratios. The highest factor of improvement values occurring for moderate spot coverage ratios that are typical for mid-M spectral types.

6. Discussion

The advantage of the CARMENES spectrograph is its large wavelength coverage and high RV precision. In this work we have investigated the wavelength dependence of RVs for the

CARMENES N_{GTO}25 sample of 215 stars. In this section we discuss our results.

6.1. CRX-gradient and CRX-length as a function of stellar parameters

Our results show that from the CARMENES $N_{\rm GTO}25$ sample of 215 stars that 39 stars show a strong or a moderate correlation between the CRX and the RV (CRX-all stars). Furthermore, a subset of 13 of these stars show a tight linear relationship (CRX-slope stars).

We demonstrate that the larger the variation is in CRX-length / $v\sin i$ the larger the variation is in CRX (i.e. ΔCRX). The highest variations in CRX-length and CRX tend to occur for the least massive stars with the steepest CRX-gradients where their activity levels are saturated. The caveat with this is that these stars have very little flux at bluer wavelenghts and may be biased. However, the very active star K2-22 also shows a very steep slope but has a spectral type of M 3.0 V. This shows that our methods can detect a CRX-RV correlation even for more rapidly rotating stars with high levels of stellar activity.

There is also a strong dependence of the CRX-length $/v \sin i$ on the Pearson's r value with the slowest rotating stars having the lowest CRX-length / $v \sin i$ values and at most moderate Pearson's r values for the CRX-RV relation. This is in agreement with the previous work of Tal-Or et al. (2018). There is also a correlation of the CRX-length $/v \sin i$ with spot to photosphere temperature contrasts where stars with lower contrasts (e.g. at late M spectral types) show higher CRX-length $/v \sin i$ values. While these results are valid for our sample of stars, a true determination of the inter-dependency between CRX-length / $v \sin i$ and the stellar spot to photosphere temperature contrast is only possible knowing the distribution and evolution of spots and other features of stellar activity on the stellar surface. As noted by Barnes et al. (2011), the latitude of a starspot (or other activity signature) will impact the activity induced RV, with higher latitude spots having a lower RV than equatorial spots. Similarly, the latitude of spots will impact the lemniscate shape (Boisse et al. 2011). We already know from our extensive investigation of stellar activity the CARMENES consortium, that every M dwarf is an individual when it comes to its activity patterns and evolution timescales.

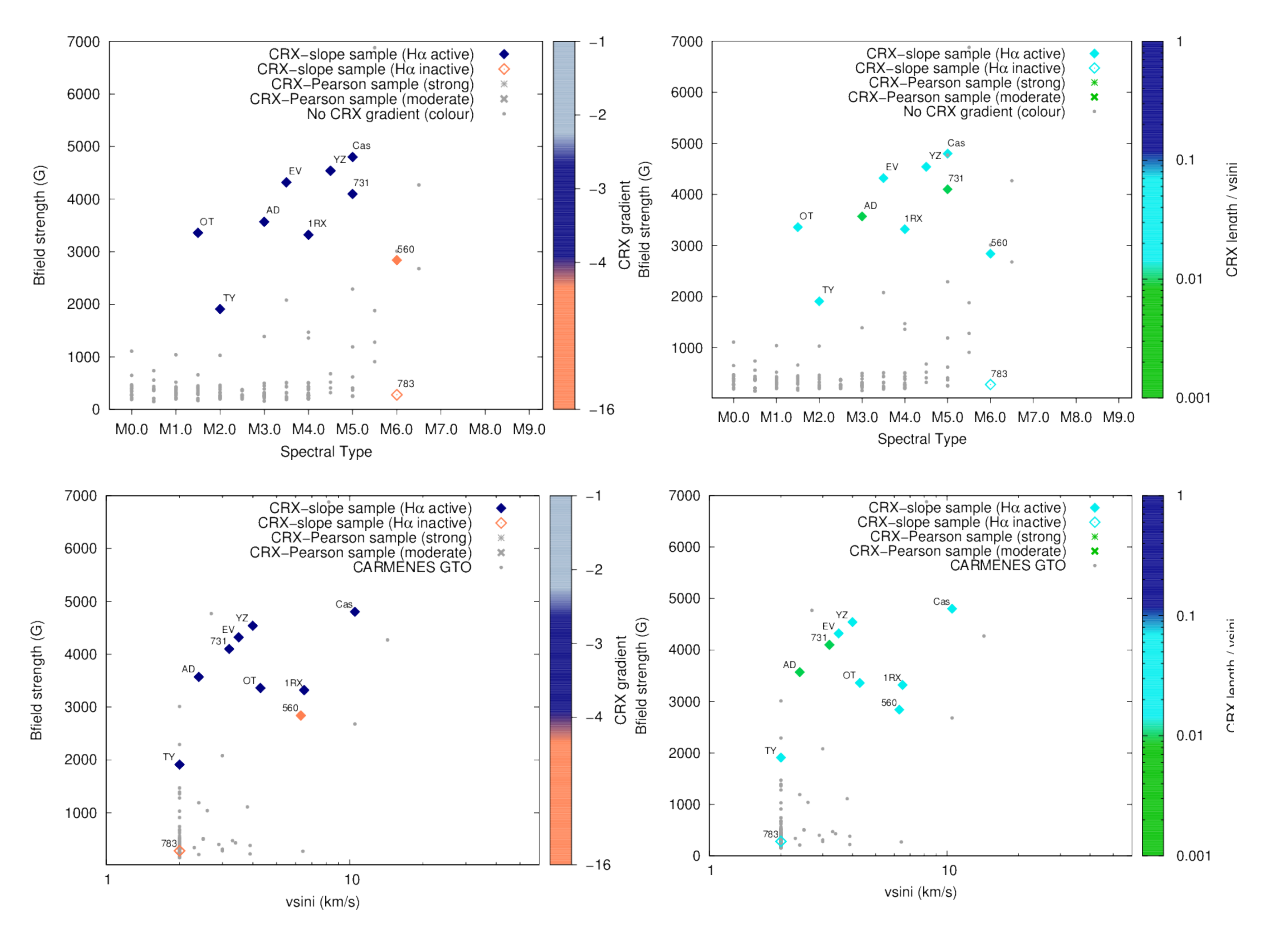


Fig. 13. Average magnetic field strength as a function of spectral type (upper panels) and $v \sin i$ (lower panels) for the CARMENES GTO sample with $N_{\rm obs} > 25$. Stars in the CRX-slope sample are indicated by diamonds and are coloured according to CRX-gradient (left panel) and CRX-length (right panel). The minimum $v \sin i$ value plotted is 2 km s^{-1} . The stars are labelled as indicated in Table A.1.

6.1.1. Dependence of CRX-gradient on stellar activity

Since there is only one star with a classification of having a shallow CRX-gradient, we restrict the discussion of our results to the stars with moderate and steep slopes. The stars in the CRX-slope sample with moderate CRX-gradients cover a range in spectral type from early-M to mid M as indicated by the navy points in Figures 8 to 13. These stars are active stars as evidenced by: (i) higher $v \sin i$ values of up to 5 km s⁻¹ for stars with early-M spectral types and a range of $v \sin i$ values from 2 to 11 km s⁻¹ at mid-M spectral types (Figure 8), (ii) a range in rotation periods from 1 to 11 days, (iii) the highest $\log(L_{\text{H}\alpha}/L_{\text{bol}})$ values (Figure 9) in the CRX-all sample of 39 stars (iv) located in the upper part of the $\log(L_{\rm H\alpha}/L_{\rm bol})$ as a function of $v \sin i$ (Figure 10), (v) lowest TiO7050 values per spectral type bin (Figure 11), (vi) saturation in X-rays (not shown), (vi) highest average magnetic field strengths as a function of spectral type and $v \sin i$ (Figure 13, upper and lower panels respectively). They also have, for our M-dwarf sample, comparatively high to moderate ΔT spot/photosphere temperature contrasts.

There are only a few stars with high CRX-gradient values and the latest spectral types of the CRX-slope sample. Despite their high-CRX-gradients, these stars exhibit moderate levels of activity (i) they have moderate to high $v \sin i$ levels (Figure 8), (ii) are the most H α active stars in the CARMENES $N_{\rm GTO}$ 25-sample for the latest spectral types (Figure 9), (iii) are located in the active part of the $\log(L_{\rm H}\alpha/L_{\rm bol})$ as a function of $v \sin i$ (Figure 10), (iv) are located in the 'hook' part of the TiO7050 per spectral

type bin (Figure 11), (v) show moderate average magnetic field strengths as a function of spectral type and $v\sin i$ (Figure 13, upper and lower panels respectively). Their moderate activity is because late-M dwarfs saturate at lower activity levels compared to early- and mid-M dwarfs (for more details see Mohanty & Basri 2003). These stars have the smallest ΔT spot/photosphere temperature contrasts and previously explained, we advise caution in the literal interpretation of these steep slopes as they may be biased due to the lack of flux at blue orders compared to the rest of the sample.

6.1.2. Dependence of CRX-length on stellar activity

The stars with the shortest CRX-length values have mid-M spectral types and show low to moderate levels of stellar activity as evidenced by (i) their low $v \sin i$ values (Figure 8) and a range of moderate rotation periods (Figure 7, (ii) are the least H α active stars (Figure 9), (iii) are located in the unsaturated part of the rotation-activity relation (Figure 10), (iv) have low to moderate average magnetic field strengths and are located on the unsaturated part of the magnetic field - rotation relation (Figure 13, lower and upper panels respectively).

Stars with moderate CRX-length values typically are early-to mid- M dwarfs with moderate to high levels of stellar activity. This is shown by (i) their increased $v \sin i$ levels and short rotation periods (Figure 8), (ii) generally the H α activity levels for their spectral types (Figure 9), (iii) that they are mostly located on the saturated part of the rotation-activity relation (Figure 10)

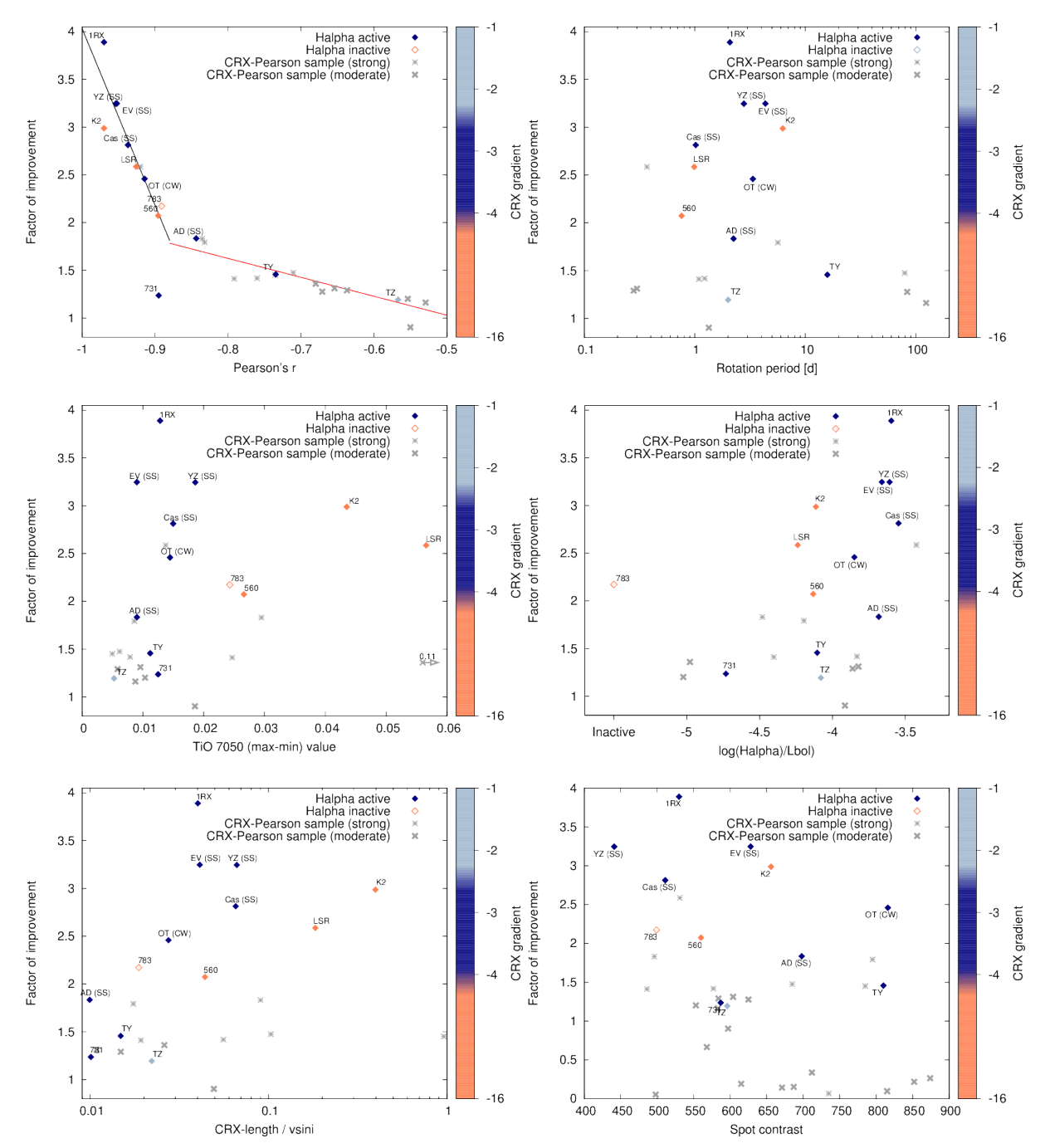


Fig. 14. Factor of improvement in the RV rms from the subtraction of the RV estimated from the RV-CRX correlation for each star in the CRX-all sample. Filled points indicate H α active stars while open points show H α inactive stars. Symbols are coloured based on CRX-gradient value or none (grey points). The factor of improvement is shown as a function of Pearson's r, stellar rotation period (upper row, left and right), stellar TiO7050 max-min value (using 95% percentiles) and normalised H α luminosity (middle row row left and right) and CRX-length / $v \sin i$ and (zoomed) spot contrast ratio (lower row left and right). The stars are labelled as indicated in Table A.1.

and X-ray distributions (not shown), (iv) highest average magnetic field strengths for their spectral types (Figure 13 upper and lower panels).

As we know that the late-M dwarfs saturate in activity we already know what to expect. The CRX-length is longest for the stars with mid- to late-M spectral types. Compared to the CARMENES $N_{\rm GTO}25$ sample, they are not the most active stars, in both H α and average magnetic field strengths, for their spectral type, but they do have moderate to fast $v \sin i$ values and short rotation periods (Figure 8). Their normalised H α levels are close

to or above the blue line (indicating very high levels of $H\alpha$ activity) in Figure 9 and are on the saturated part of the rotation-activity relation Figure 10 and 13. They also cover the 'hook' in the TiO distribution with spectral type.

6.2. Average magnetic field strength

The average magnetic field strengths were computed from the telluric corrected co-added templates with exceptional high signal to noise values (Reiners et al. 2022). The CRX-gradient

shows moderate values for the stars with the highest average magnetic field strengths at mid-M spectral types. The average magnetic field strength have been shown by Haywood et al. (2014, 2022) to be a proxy of RV variations in the Sun and other stars in agreement with Meunier et al. (2010). Recently, the work of Ruh et al. (2024) investigated the RV jitter and its relation to the average magnetic field strength. They showed that M dwarfs with excess activity-rotation induced RV jitter have magnetic field filling factors that are dominated by a component with a strength of 2 to 4 kG.

6.3. Correlations with Bisector Inverse Span (BIS)

All of the CRX-all stars have a strong or moderate (anti-) correlations between CRX and Moment 1 indicators such as RV. Recent models of stellar activity, and its impact on the line moments Barnes et al. (2024), show that there is a high likelihood of having correlations between odd numbered moments such as Moment 1 (e.g. RV) and Moment 3 (e.g. the BIS). While the CRX-index and BIS measure different aspects of the stellar spectra, it is important to also note that the BIS also includes a chromatic effect. This is because the skewness of the line profile is caused by the different velocity patterns as a function of formation depth, with redder lines being weaker.

Given the similarity of the lemniscate shape of the CRX and the BIS (see for e.g. Boisse et al. 2011), we additionally investigate the statistical correlation between the CRX and BIS (Moment 3 line moment). We use Pearson's r for the 39 stars in the CRX-all sample. Our results are shown in Table A.1 and confirm that Moment 1 and Moment 3 are linked with 13 stars having either a strong or a moderate Pearson's r value between the CRX and BIS. The 3 stars that show the highest factor of improvement also show a strong correlation between CRX and BIS (see Appendix Table A.1). This is in agreement with our previous observational results for the mid M dwarf EV Lac (Jeffers et al. 2022), the results of Schöfer et al. (2022) for four stars in the CARMENES sample.

Recently, Lafarga et al. (2021) investigated the optimal activity indicators to identify activity induced RV signals in M dwarf stars with a range of activity levels. They report that the CRX and BIS are the most effective indicators for tracing activity in high-mass and high-activity (measured by $H\alpha$) M dwarfs. A total of 9 CRX-slope and 4 CRX-Pearson stars are also included in their sample, where for each of these star the stellar rotation period is detected in the RV (9 CRX-slope, 4 CRX-Pearson) and the CRX (9 CRX-slope, 1 CRX-Pearson). A total of 6 CRX-slope stars and 3 CRX-Pearson stars have both the a periodic signal detected at the stellar rotation period in BIS.

Previously, the results of Saar & Donahue (1997) reported that the BIS span varies as $(v \sin i)^{3.3}$. In Figure 15 we show the distribution of $v \sin i$ of the CRX-all sample where the distribution of the stars with a strong or a moderate correlation between the CRX-index and the BIS are highlighted. Our results show that BIS is a significant parameter, at moderate $v \sin i$ rates and even at low $v \sin i$ levels. While models of fixed starspots are important, a comprehensive analysis also needs to take into account the variations in the latitude, longitude and lifetimes of the spot distributions over the time span of data collection.

6.4. Subtraction of the CRX

The subtraction of a linear fit of the CRX-RV anti-correlation from the RV results in a reduction of the RV rms by a factor of

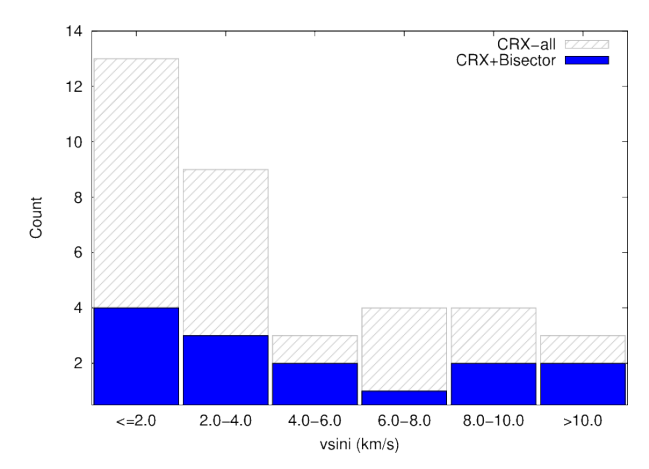


Fig. 15. The $v \sin i$ distribution of all 39 stars in the CRX-all sample (CRX-slope and CRX-Pearson) shown as grey shaded bars. The stars with a strong or a moderate correlation of the CRX with BIS are shown in blue.

up to 4. There is a tight correlation of factor of improvement with Pearson's r for both the CRX-slope and Pearson-all samples, where the best stars typically have rotation periods of several days (Figure 14 top panels), low levels of Δ TiO and very high H_{α} values (Figure 14 middle panels) and moderate CRX-length / $v \sin i$ values and low to moderate M dwarf spot contrasts. The moderate rotation periods and low Δ TiO values point to stable spot feature, though the high H_{α} values could result from plage regions appearing dark at the limb centre as suggested by Johnson et al. (2021).

Whether the star has a moderate or a steep CRX-gradient does not influece the factor of improvement values. However, in both the Δ TiO and the $H\alpha$ activity relations, the CRX-slope stars with the steepest gradients occupy a separate branch or region compared to the CRX-slope stars with moderate gradients. Furthermore, we show that all of the CRX-slope stars with moderate gradients have CRX-length / $v\sin i$ values that are low to moderate (with the best factor of improvement values) and that the steepest gradients have the longest lengths. The stars with the longest CRX-length values are in the saturated regime of the rotation-activity plot and have moderate CRX slopes. These relations are summarised in Figure 14 and Table 5.

6.4.1. Planet detection thresholds

We have demonstrated that the improvement in the RV rms by removing the contribution of the CRX can be up to a factor of nearly four. The implications that this has for improving the detectability of small exoplanets was simulated using the dataset of EV Lac. An exoplanetary signal is first injected in the uncorrected data and then the activity contribution is removed (Cardona Guillén et al. 2023). With the linear correction factor it is possible to detect exoplanets that are approximately 2.5 times less massive compared to the same dataset but without the correction. The exoplanetary signal can be identified even if it is not a significant signal in the original dataset. We will explore this further in forthcoming papers.

Other techniques that exploit the wavelength dependence of activity induced RVs include the work by Collier Cameron et al. (2021). They present test simulations by adding injected signals of low-mass planets to 5 years of HARPS Sun-as-a-Star observations of the solar spectrum where planets can be recovered with a precision of $\sim 6.6~\rm cm~s^{-1}$.

Table 5. Summary of relations derived in this work

| Relation | Figure | Equ No (text) |
|---|--------|---------------|
| $\Delta T = 0.47 T_{\text{phot}} - 926.97$ | 3 | 1 |
| $\log(CRX_{\text{max}} - CRX_{\text{min}}) = 1.08\log(RV_{\text{max}} - RV_{\text{min}}) + 0.336$ | 5 | |
| $\log(CRX_{\text{length}}/v\sin i) = -1.71r - 2.846$ | 6 | |
| $\log(CRX_{\text{length}}/v\sin i) = 9.7 \times 10^{-4}\Delta T - 0.967$ | 6 | |
| $\log(CRX_{\text{length}}/v\sin i) = -0.283\log P_{\text{rot}} - 1.585$ | 6 | |
| $\log \tau = (0.58 \pm 0.04) + (0.28 \pm 0.01)(V - Ks)$ | 12 | 2 |
| $\log \tau = (2.30 \pm 0.06) - (1.38 \pm 0.245)(M/M_{\odot}) + (0.22 \pm 0.19)(M/M_{\odot})^{2}$ | 12 | 3 |
| Factor of Improvement = $-18.51r - 14.48$ $(r < -0.80)$ | 14 | 4 |
| $= -1.98r + 0.04 \qquad (r > -0.80)$ | 14 | 4 |

Notes. where ΔT is the Spot / Photospheric temperature contrast ratio and r is Pearson's r

In addition to using the wavelength dependence of RVs, there are currently a large number of methods in the literature to remove the impact of stellar activity. An excellent summary of these methods is presented by Meunier (2021) (see their Table 1). Also Zhao et al. (2022) presented the results of a comparison of different methods (expanding from the work of Dumusque et al. (2017)) and concluded that no method is yet performing better than classical linear decorrelation, further supporting the results we obtained in this work.

6.4.2. Surface mapping

The large-scale magnetic field geometry has been reconstructed for a total of 6 stars in the CRX-all sample. From these 6 stars, YZ CMi and EV Lac are also part of the RV_{corr}3 stars with the highest reduction in RV rms after the subtraction of the CRX. V388 Cas, AD Leo and OT Ser are CRX-slope stars and AU Mic is a CRX-Pearson (moderate) star. The mid-M dwarfs YZ CMi and EV Lac consistently show an axisymmetric, predominantly poloidal and simple large-scale magnetic field geometry that does not change significantly over time periods of approximately 1 year (Donati et al. 2008; Morin et al. 2008b, 2010). The long-term stability of YZ CMi enabled Baroch et al. (2020) to fit CARMENES data with one stable starspot. Recently, Jeffers et al. (2022) also reconstructed several low resolution surface brightness maps of EV Lac using CARMENES data, and also found a long-term stable component with small-scale variability which is consistent with EV Lac's TESS light curve.

The remaining 3 stars in the CRX-all sample with large-scale magnetic field maps show a variety of geometries. The mid-M dwarf V388 Cas exhibits a comparably simple large-scale magnetic field geometry as reconstructed for YZ CMi and EV Lac which is also axisymmetric and predominantly poloidal. The large-scale magnetic field geometry of the mid-M dwarf AD Leo shows strong and simple magnetic features, which are mostly poloidal and axisymmetric and with low level variations over the time span of 1 year. On the other hand, the early-M dwarf OT Ser shows latitudinal rings of mixed polarities that are axisymmetric and dominated by the poloidal component but with also a significant toroidal component (Donati et al. 2008; Morin et al. 2008b, 2010).

The active planet-hosting star AU Mic, which is a CRX-Pearson moderate star in this work, has been the focus of an intensive observational campaign to reconstruct its surface activity patterns (Klein et al. 2021, 2022). AU Mic has surface brightness features that evolve rapidly, which is consistent with its young age of 22 Myr and frequent flaring events (Robinson et al. 2001). It cannot be excluded that the reason why AU Mic is not a CRX-slope star is because its stellar activity features evolved on a much more rapid timescale compared to the observational cadence of the CARMENES data of AU Mic and which may explain the curved nature of AU Mic's CRX-RV relation (see Figure A.3) and (Cale et al. 2021).

These Zeeman Doppler Imaging (ZDI) observations point to that (1) early-M dwarfs have weak but complex fields and consequently activity patterns, (2) mid-M dwarfs have less complex but strong magnetic fields and (3) late-M dwarfs can have either of these configurations. The results from brightness (Doppler) imaging typically exhibit more complex spot patterns for all M spectral types (Barnes & Collier Cameron 2001; Barnes et al. 2004, 2015b, for example) but these results are biased towards stars with $v \sin i$ values that are in excess of 15–20km s⁻¹.

6.5. Sampling of data

One point to consider is that the observations of the CARMENES GTO stars have been secured with the main aim of detecting close-in orbiting exoplanets and not characterising the stellar activity of the target stars. This means that there can be gaps in the observational timeseries of longer than several stellar rotation periods which is the timescale that we expect stellar activity features such as spots and plage region to evolve.

If the stellar activity features, and consequently the CRX, have evolved over this time frame then determining correlations and removing the contribution of the CRX will be biased by the time sampling of the dataset. For example, the very detailed analysis of EV Lac by Jeffers et al. (2022) showed that it is possible to see additional (anti-)correlations between the line moments or parameters with smaller data sets that cover only a few stellar rotation periods and where the features of stellar activity have not significantly evolved. In this work we have shown that the subtraction of the CRX from the RVs works optimally for moderate rotation periods, which is likely to result from a combination of stable global starspot patterns which are more likely to be well sampled by our CARMENES data.

For very active stars, with higher rotation periods, this could mean that the stellar activity features have evolved significantly over the timespan of the observations whereas the more stable activity patterns are less impacted by the cadence of the observations. In the future we will investigate if the more rapidly evolving stellar activity can be mitigated using densely sampled observations covering a large wavelength range, such is as used by the RedDots exoplanet search program (Jeffers et al. 2020).

7. Conclusions

In this work we have investigated the wavelength dependence of high-precision RV measurements via the CRX. We conclude the following:

- Approximately 17% of stars in the Carmenes GTO sample are CRX-all stars (i.e. stars with strong-moderate RV Pearson's r correlations of CRX-index vs RV).
- Dependence on stellar activity diagnostics shows that CRXall stars have low to moderate activity levels and cover the full range of M dwarf spectral types from M1.5 to M8.5.
- The variation of RVs with wavelength can be used to remove the impact of stellar activity with an improvement in RV rms of up to a factor of 4. The optimal targets are moderately active stars.
- The correction effectiveness is related to how stable and structured the activity patterns are, though more active stars would be feasible with regular cadence or high density sampled high-precision RVs.

The power of using the wavelength dependent information contained in the spectra themselves is that it is an instantaneous decorrelation.

8. Data availability

The Figures contained in Appendix A are only available online at https://zenodo.org/records/14013877.

Acknowledgements. We would like to thank the referee for their very insightful and constructive comments which helped to improve the clarity of the paper. This publication is based on observations collected under the CARMENES Legacy+ project. CARMENES is an instrument at the Centro Astronómico Hispano en Andalucía (CAHA) at Calar Alto (Almería, Spain), operated jointly by the Junta de Andalucía and the Instituto de Astrofísica de Andalucía (CSIC). CARMENES was funded by the Max-Planck-Gesellschaft (MPG), the Consejo Superior de Investigaciones Científicas (CSIC), the Ministerio de Economía y Competitividad (MINECO) and the European Regional Development Fund (ERDF) through projects FICTS-2011-02, ICTS-2017-07-CAHA-4, and CAHA16-CE-3978, and the members of the CARMENES Consortium (Max-Planck-Institut für Astronomie, Instituto de Astrofísica de Andalucía, Landessternwarte Königstuhl, Institut de Ciències de l'Espai, Institut für Astrophysik Göttingen, Universidad Complutense de Madrid, Thüringer Landessternwarte Tautenburg, Instituto de Astrofísica de Canarias, Hamburger Sternwarte, Centro de Astrobiología and Centro Astronómico Hispano-Alemán), with additional contributions by the MINECO, the Deutsche Forschungsgemeinschaft (DFG) through the Major Research Instrumentation Programme and Research Unit FOR2544 "Blue Planets around Red Stars", the Klaus Tschira Stiftung, the states of Baden-Württemberg and Niedersachsen, and by the Junta de Andalucía. This work was based on data from the CARMENES data archive at CAB (CSIC-INTA). We acknowledge financial support from the Agencia Estatal de Investigación (AEI/10.13039/501100011033) of the Ministerio de Ciencia e Innovación and the ERDF "A way of making Europe" through projects PID2021-125627OB-C31, PID2019-109522GB-C5[1:4] and the Centre of Excellence "Severo Ochoa" and "María de Maeztu" awards to the Instituto de Astrofísica de Canarias (CEX2019-000920-S), Instituto de Astrofísica de Andalucía (CEX2021-001131-S), and Centro de Astrobiología (MDM-2017-0737). This work was also funded by the Generalitat de Catalunya/CERCA programme, and the DFG through the priority program SPP 1992 'Exploring the Diversity of Extrasolar Planets' (Jeffers, JE 701/5-1).

```
References
```

```
Amado, P. J. & Zboril, M. 2002, A&A, 381, 517
Barnes, J. R. & Collier Cameron, A. 2001, MNRAS, 326, 950
Barnes, J. R., James, D. J., & Collier Cameron, A. 2004, MNRAS, 352, 589
Barnes, J. R., Jeffers, S. V., Haswell, C. A., et al. 2024, MNRAS, 534, 1257
Barnes, J. R., Jeffers, S. V., Haswell, C. A., et al. 2017, MNRAS, 471, 811
Barnes, J. R., Jeffers, S. V., & Jones, H. R. A. 2011, MNRAS, 412, 1599
Barnes, J. R., Jeffers, S. V., Jones, H. R. A., et al. 2015a, ApJ, 812, 42
Barnes, J. R., Jeffers, S. V., Jones, H. R. A., et al. 2015b, , $12, 42
Baroch, D., Morales, J. C., Ribas, I., et al. 2020, A&A, 641, A69
Bauer, F. F., Zechmeister, M., Kaminski, A., et al. 2020, A&A, 640, A50
Bean, J. 2020, American Astronomical Society Meeting Abstracts, 235, 225.04
Bellotti, S., Petit, P., Morin, J., et al. 2022, A&A, 657, A107
Berdyugina, S. V. 2005, Living Reviews in Solar Physics, 2, 8
Boisse, I., Bouchy, F., Hébrard, G., et al. 2011, A&A, 528, A4
Caballero, J. A., Cortés-Contreras, M., Alonso-Floriano, F. J., et al. 2016, Cam-
bridge Workshop on Cool Stars, Stellar Systems, and the Sun, 148
Caballero, J. A., González-Álvarez, E., Brady, M., et al. 2022, A&A, 665, A120
Cale, B. L., Reefe, M., Plavchan, P., et al. 2021, AJ, 162, 295
Cardona Guillén, C., Béjar, V. J. S., & Lodieu, N. 2023, A&A submitted
Carmona, A., Delfosse, X., Bellotti, S., et al. 2023, A&A, 674, A110
Collier Cameron, A., Ford, E. B., Shahaf, S., et al. 2021, MNRAS, 505, 1699
Crass, J., Gaudi, B. S., Leifer, S., et al. 2021, arXiv e-prints, arXiv:2107.14291
Desort, M., Lagrange, A. M., Galland, F., Udry, S., & Mayor, M. 2007, A&A,
   473, 983
Díez Alonso, E., Caballero, J. A., Montes, D., et al. 2019, A&A, 621, A126
Donati, J. F., Morin, J., Petit, P., et al. 2008, MNRAS, 390, 545
Dravins, D., Lindegren, L., & Nordlund, A. 1981, A&A, 96, 345
Dreizler, S., Luque, R., Ribas, I., et al. 2024, A&A, 684, A117
Dumusque, X., Boisse, I., & Santos, N. C. 2014, ApJ, 796, 132
Dumusque, X., Borsa, F., Damasso, M., et al. 2017, A&A, 598, A133
Fuhrmeister, B., Czesla, S., Schmitt, J. H. M. M., et al. 2019, A&A, 623, A24
Haywood, R. D., Collier Cameron, A., Queloz, D., et al. 2014, MNRAS, 443,
Haywood, R. D., Milbourne, T. W., Saar, S. H., et al. 2022, ApJ, 935, 6
Jeffers, S. V. 2005, MNRAS, 359, 729
Jeffers, S. V., Barnes, J. R., Jones, H. R. A., et al. 2014, MNRAS, 438, 2717
Jeffers, S. V., Barnes, J. R., Schöfer, P., et al. 2022, A&A, 663, A27
Jeffers, S. V. & Donati, J. F. 2008, MNRAS, 390, 635
Jeffers, S. V., Dreizler, S., Barnes, J. R., et al. 2020, Science, 368, 1477
Jeffers, S. V., Schöfer, P., Lamert, A., et al. 2018, A&A, 614, A76
Johnson, L. J., Norris, C. M., Unruh, Y. C., et al. 2021, MNRAS, 504, 4751
Jurgenson, C., Fischer, D., McCracken, T., et al. 2016, Society of Photo-Optical
   Instrumentation Engineers (SPIE) Conference Series, 9908, 99086T
Klein, B., Donati, J.-F., Moutou, C., et al. 2021, MNRAS, 502, 188
Klein, B., Zicher, N., Kavanagh, R. D., et al. 2022, MNRAS, 512, 5067
Kossakowski, D., Kürster, M., Henning, T., et al. 2022, A&A, 666, A143
Lafarga, M., Ribas, I., Lovis, C., et al. 2020, A&A, 636, A36
Lafarga, M., Ribas, I., Reiners, A., et al. 2021, A&A, 652, A28
Lagrange, A. M., Desort, M., & Meunier, N. 2010, A&A, 512, A38
Liebing, F., Jeffers, S. V., Reiners, A., & Zechmeister, M. 2021, A&A, 654, A168
Lisogorskyi, M., Jones, H. R. A., & Feng, F. 2019, MNRAS, 485, 4804
Luque, R., Fulton, B. J., Kunimoto, M., et al. 2022, A&A, 664, A199
Martioli, E., Hébrard, G., Correia, A. C. M., Laskar, J., & Lecavelier des Etangs,
   A. 2021, A&A, 649, A177
Meunier, N. 2021, arXiv e-prints, arXiv:2104.06072
Meunier, N., Desort, M., & Lagrange, A. M. 2010, A&A, 512, A39
Mohanty, S. & Basri, G. 2003, ApJ, 583, 451
Morales, J. C., Mustill, A. J., Ribas, I., et al. 2019, Science, 365, 1441
Morin, J., Donati, J. F., Forveille, T., et al. 2008a, MNRAS, 384, 77
Morin, J., Donati, J. F., Petit, P., et al. 2008b, MNRAS, 390, 567
Morin, J., Donati, J. F., Petit, P., et al. 2010, MNRAS, 407, 2269
Nagel, E., Czesla, S., Kaminski, A., et al. 2023, A&A, 680, A73
Newton, E. R., Mondrik, N., Irwin, J., Winters, J. G., & Charbonneau, D. 2018,
   AJ, 156, 217
O'Neal, D., Neff, J. E., Saar, S. H., & Cuntz, M. 2004, AJ, 128, 1802
Panja, M., Cameron, R., & Solanki, S. K. 2020, ApJ, 893, 113
Pepe, F., Cristiani, S., Rebolo, R., et al. 2021, A&A, 645, A96
Perdelwitz, V., Mittag, M., Tal-Or, L., et al. 2021, A&A, 652, A116
Plavchan, P., Barclay, T., Gagné, J., et al. 2020, Nature, 582, 497
Queloz, D., Henry, G. W., Sivan, J. P., et al. 2001, A&A, 379, 279
Quirrenbach, A., Amado, P. J., Ribas, I., et al. 2018, Proc. SPIE, 10702,
   107020W
Quirrenbach, A., CARMENES Consortium, Amado, P. J., et al. 2020, Society of
   Photo-Optical Instrumentation Engineers (SPIE) Conference Series, 11447,
Radica, M., Artigau, É., Lafreniére, D., et al. 2022, MNRAS, 517, 5050
Reiners, A., Bean, J. L., Huber, K. F., et al. 2010, ApJ, 710, 432
Reiners, A., Shulyak, D., Käpylä, P. J., et al. 2022, Â&A, 662, A41
```

Reiners, A., Zechmeister, M., Caballero, J. A., et al. 2018, A&A, 612, A49

- Ribas, I., Reiners, A., Zechmeister, M., et al. 2023, A&A, 670, A139
- Robinson, R. D., Linsky, J. L., Woodgate, B. E., & Timothy, J. G. 2001, ApJ, 554, 368
- Ruh, H., Zechmeister, M., & Reiners, A. 2024, A&A submitted
- Saar, S. H. & Donahue, R. A. 1997, ApJ, 485, 319
- Sarkis, P., Henning, T., Kürster, M., et al. 2018, AJ, 155, 257
- Schöfer, P., Jeffers, S. V., Reiners, A., et al. 2019, A&A, 623, A44
- Schöfer, P., Jeffers, S. V., Reiners, A., et al. 2022, A&A, 663, A68
- Shan, Y., Revilla, D., Skrzypinski, S. L., et al. 2024, A&A, 684, A9
- Suárez Mascareño, A., Faria, J. P., Figueira, P., et al. 2020, A&A, 639, A77
- Suárez Mascareño, A., González-Álvarez, E., Zapatero Osorio, M. R., et al. 2023, A&A, 670, A5
- Suárez Mascareño, A., Rebolo, R., González Hernández, J. I., & Esposito, M. 2015, MNRAS, 452, 2745
- Suárez Mascareño, A., Rebolo, R., González Hernández, J. I., & Esposito, M. 2017, MNRAS, 468, 4772
- Suárez Mascareño, A., Rebolo, R., González Hernández, J. I., et al. 2018, A&A, 612, A89
- Tal-Or, L., Zechmeister, M., Reiners, A., et al. 2018, A&A, 614, A122 Vogt, S. S. 1979, PASP, 91, 616

- Waite, I. A., Marsden, S. C., Carter, B. D., et al. 2015, MNRAS, 449, 8 Waite, I. A., Marsden, S. C., Carter, B. D., et al. 2017, MNRAS, 465, 2076
- Wittrock, J. M., Dreizler, S., Reefe, M. A., et al. 2022, AJ, 164, 27
- Wright, N. J., Newton, E. R., Williams, P. K. G., Drake, J. J., & Yadav, R. K. 2018, MNRAS, 479, 2351
- Zechmeister, M., Anglada-Escudé, G., & Reiners, A. 2014, A&A, 561, A59
- $Zechmeister,\,M.,\,Dreizler,\,S.,\,Ribas,\,I.,\,et\,al.\,\,2019,\,A\&A,\,627,\,A49$
- Zechmeister, M., Reiners, A., Amado, P. J., et al. 2018, A&A, 609, A12
- Zhao, L. L., Fischer, D. A., Ford, E. B., et al. 2022, AJ, 163, 171

Appendix A: Supplementary information

Table A.1. Derived CRX parameters of the CRX-all stars sample.

| Karmn | Name | Label (plots) | Sp. type | CRX gradient (Np^{-1}) | length (ms ⁻¹) | Pearson r | Factor RV red. | Spot/phot. cont. (K) | BIS (mod / strong) |
|------------|-----------------------|------------------|-------------|----------------------------|----------------------------|-----------|-------------------|----------------------|--------------------|
| | | | CRX-slope | sample | | | | | |
| J01033+623 | V388 Cas | Cas | M5.0 V | -2.67 ± 0.20 | 686 | -0.94 | 2.81 | 511 | M |
| J02002+130 | TZ Ari | TZ | M3.5 V | -1.16 ± 0.18 | 44 | -0.57 | 1.19 | 596 | |
| J04198+425 | LSR J0419+4233 | LSR^{\diamond} | M8.5 V | -4.64 ± 0.33 | 658 | -0.93 | 2.59 | 202 | |
| J05019+011 | 1RXS J050156.7+010845 | 1RX | M4.0 V | -3.03 ± 0.15 | 261 | -0.97 | 3.89 | 530 | S |
| J07403-174 | LP 783-002 | 783◊ | M6.0 V | -16.98 ± 1.21 | 37 | -0.89 | 2.17 | 499 | |
| J07446+035 | YZ CMi | YZ | M4.5 V | -2.92 ± 0.13 | 265 | -0.95 | 3.25 | 441 | S |
| J10196+198 | AD Leo | AD | M3.0 V | -3.64 ± 0.25 | 43 | -0.84 | 1.83 | 698 | S |
| J10584-107 | LP 731-076 | 731 | M5.0 V | -3.51 ± 0.69 | 32 | -0.90 | 1.24 | 587 | |
| J14321+081 | LP 560-035 | 560◊ | M6.0 V | -8.68 ± 0.58 | 277 | -0.90 | 2.07 | 560 | |
| J15218+209 | OT Ser | OT | M1.5 V | -3.65 ± 0.23 | 118 | -0.91 | 2.46 | 816 | S |
| J16102-193 | K2-33 | K2 | M3.0 V | -8.49 ± 0.45 | 2897 | -0.97 | 2.99 | 656 | |
| J18174+483 | TYC 3529–1437–1 | TY | M2.0 V | -2.97 ± 0.33 | 30 | -0.73 | 1.46 | 810 | M |
| J22468+443 | EV Lac | EV | M3.5 V | -3.16 ± 0.10 | 144 | -0.95 | 3.25 | 628 | S |
| | | (| CRX-Pears | on strong | | | | | |
| J04173+088 | LTT 11392 | * | M4.5 V | | 1447 | -0.92 | 2.43 | 531 | |
| J06396-210 | LP 780–032 | * | M4.0 V | | 206 | -0.71 | 1.47 | 685 | M |
| J08536-034 | LP 666–009 | * | M9.0 V | | 588 | -0.86 | | 202 | |
| J09033+056 | NLTT 20861 | * | M7.0 V | | 874 | -0.84 | 1.83 | 496 | S |
| J11044+304 | LSPM J1104+3027 | * | M3.0 V | | 105 | -0.73 | | 735 | |
| J11201-104 | LP 733-099 | * | M2.0 V | | 63 | -0.83 | 1.79 | 795 | S |
| J13536+776 | RX J1353.6+7737 | * | M4.0 V | | 496 | -0.76 | 1.42 | 577 | |
| J16555-083 | VB 8 | * | M7.0 V | | 104 | -0.79 | 1.41 | 486 | |
| J23556-061 | GJ 912 | * | M2.5 V | | 1918 | -0.74 | 1.45 | 785 | |
| | | CI | RX-Pearsor | n moderate | | | | | |
| J02358+202 | BD+19 381 | × | M2.0 V | | 8 | -0.51 | | 815 | M |
| J04153-076 | omi02 Eri C | × | M4.5 V | | 26 | -0.62 | | 568 | |
| J06318+414 | LP 205-044 | × | M5.0 V | | 635 | -0.65 | 1.31 | 604 | |
| J06594+193 | GJ 1093 | × | M5.0 V | | 13 | -0.55 | 1.2 | 553 | |
| J07582+413 | GJ 1105 | × | M3.5 V | | 8 | -0.52 | | 687 | |
| J10482-113 | LP 731-058 | × | M6.5 V | | 21 | -0.69 | | 498 | |
| J13450+176 | BD+18 2776 | × | M0.0 V | | 28 | 0.55 | | 874 | |
| J15412+759 | UU UMi | × | M3.0 V | | 3165 | -0.67 | 1.28 | 625 | |
| J16581+257 | BD+25 3173 | × | M1.0 V | | 15 | -0.68 | | 852 | |
| J18022+642 | LP 071-082 | × | M5.0 V | | 168 | -0.64 | 1.29 | 584 | |
| J18027+375 | GJ 1223 | × | M5.0 V | | 11 | -0.53 | 1.16 | 583 | |
| J19216+208 | GJ 1235 | × | M4.5 V | | 11 | -0.51 | | 615 | |
| J19255+096 | LSPM J1925+0938 | × | M8.0 V | | 903 | -0.68 | 1.36 | 249 | |
| J19422-207 | 2MASS J19421282 | | | | | | | | |
| | -2045477 | × | M5.1 V | | 306 | -0.55 | | 597 | |
| J20451-313 | AU Mic | × | M0.5 V | | 262 | -0.61 | | 712 | M |
| J23064-050 | 2MUCD 12171 | × | M8.0 V | | 722 | 0.62 | ••• | 296 | |
| 323001 030 | | | | | | | | | |

Notes. (**) Caution should be exercised in the interpretation of these CRX-gradient values as for the later spectral types there is less flux in the bluer wavelengths and may bias the result.

Article number, page 19 of 26

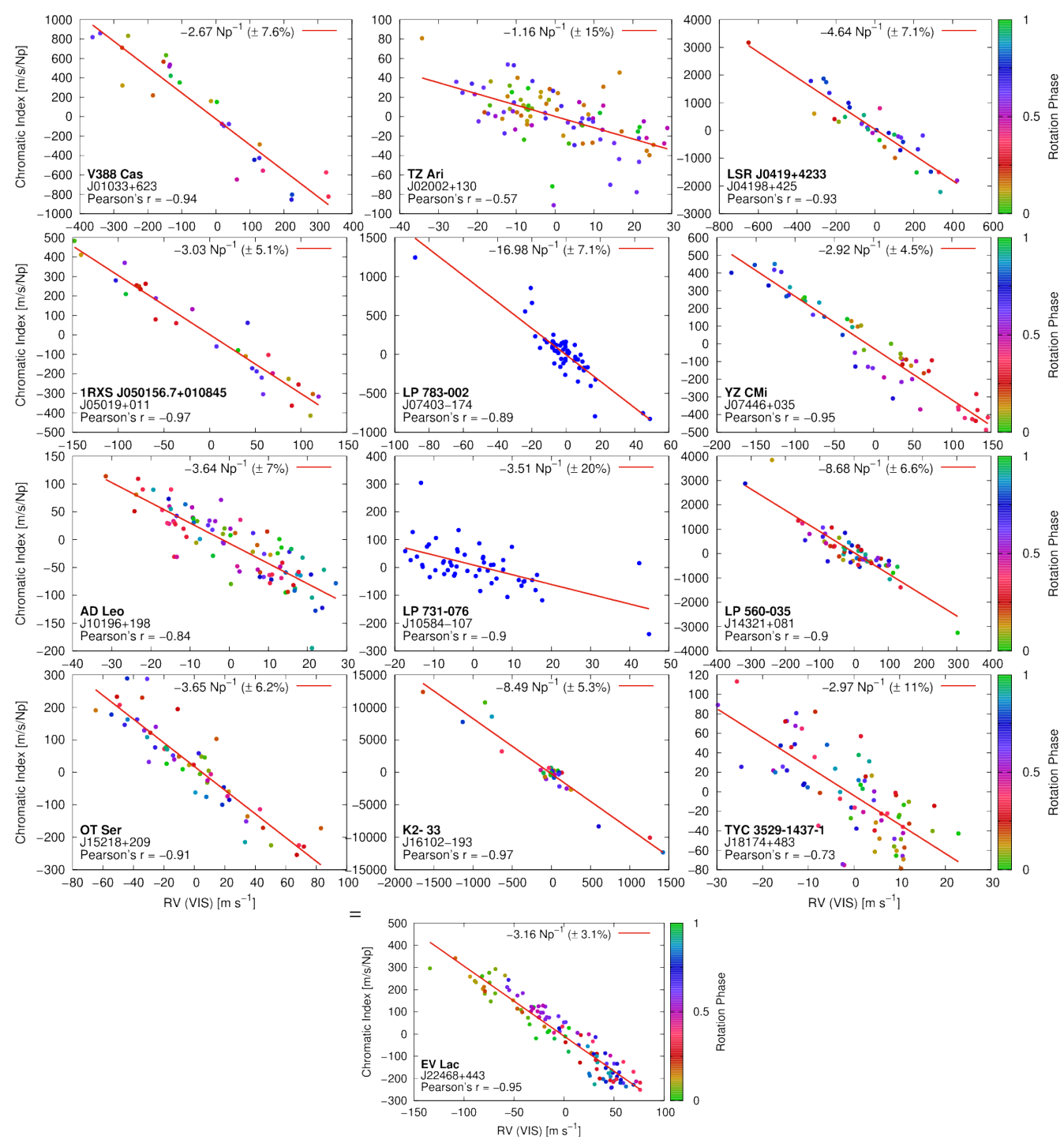


Fig. A.1. CRX as a function of RV for each star in the CRX-slope sample. Points are coloured by rotational phase derived from the rotation periods of Shan et al. (2024). Stars with only blue coloured points do not have a known rotation period.

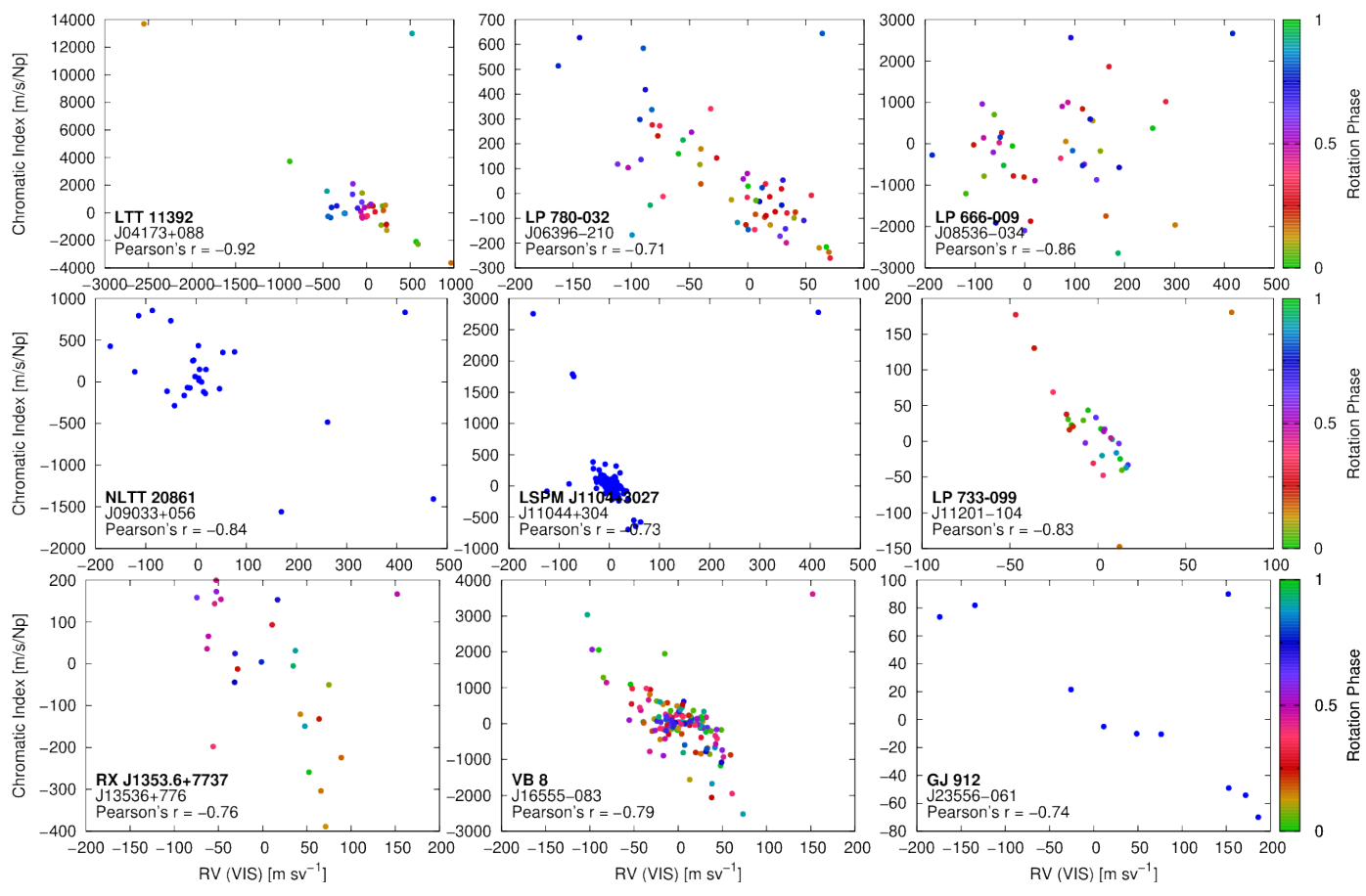


Fig. A.2. CRX as a function of RV for each star in the CRX-Pearson (strong) sample. Points are coloured by rotational phase derived from the rotation periods of Shan et al. (2024). Stars with only blue coloured points do not have a known rotation period.

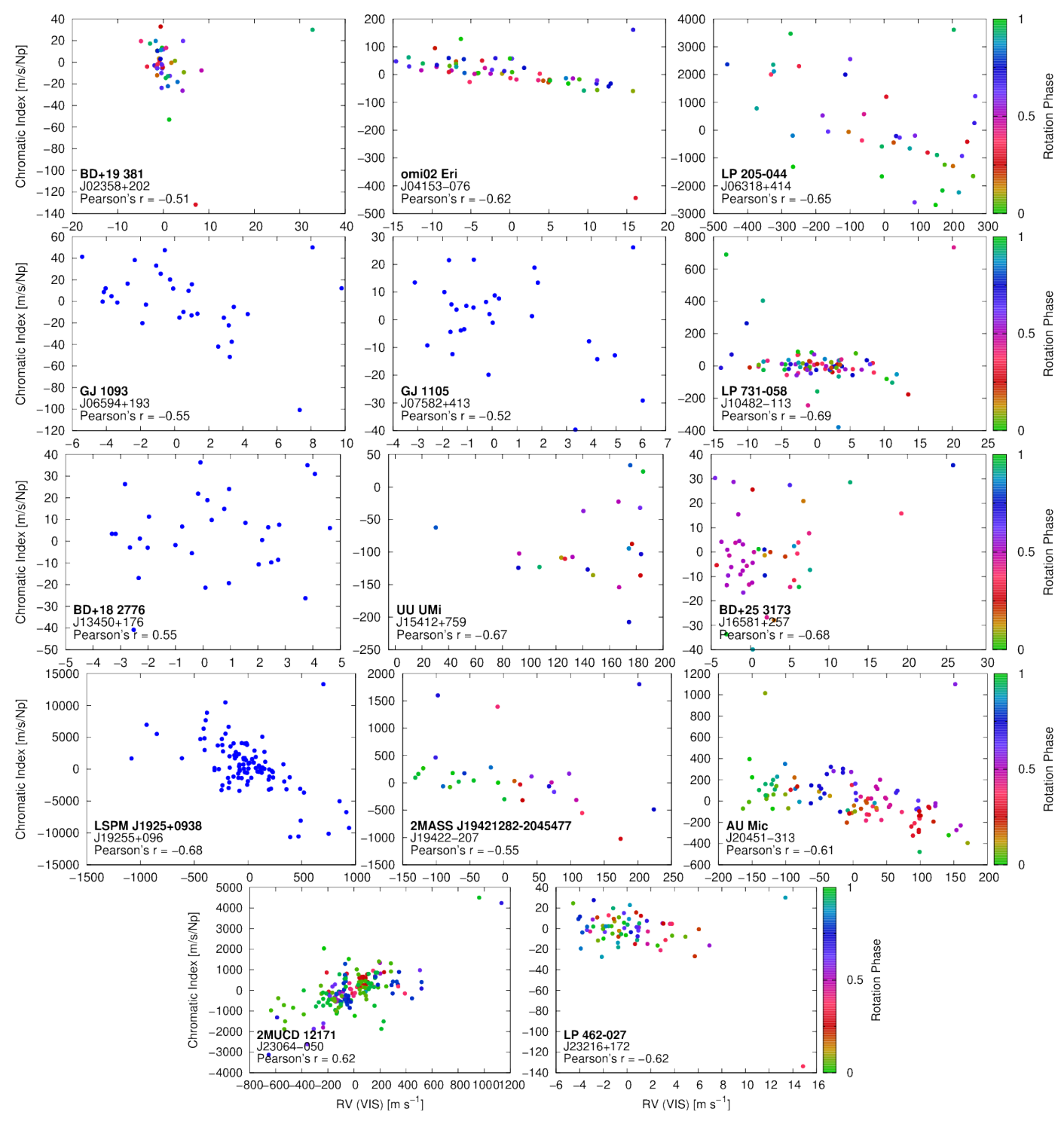


Fig. A.3. CRX as a function of RV for each star in the CRX-Pearson (moderate) sample. Points are coloured by rotational phase derived from the rotation periods of Shan et al. (2024). Stars with only blue coloured points do not have a known rotation period.

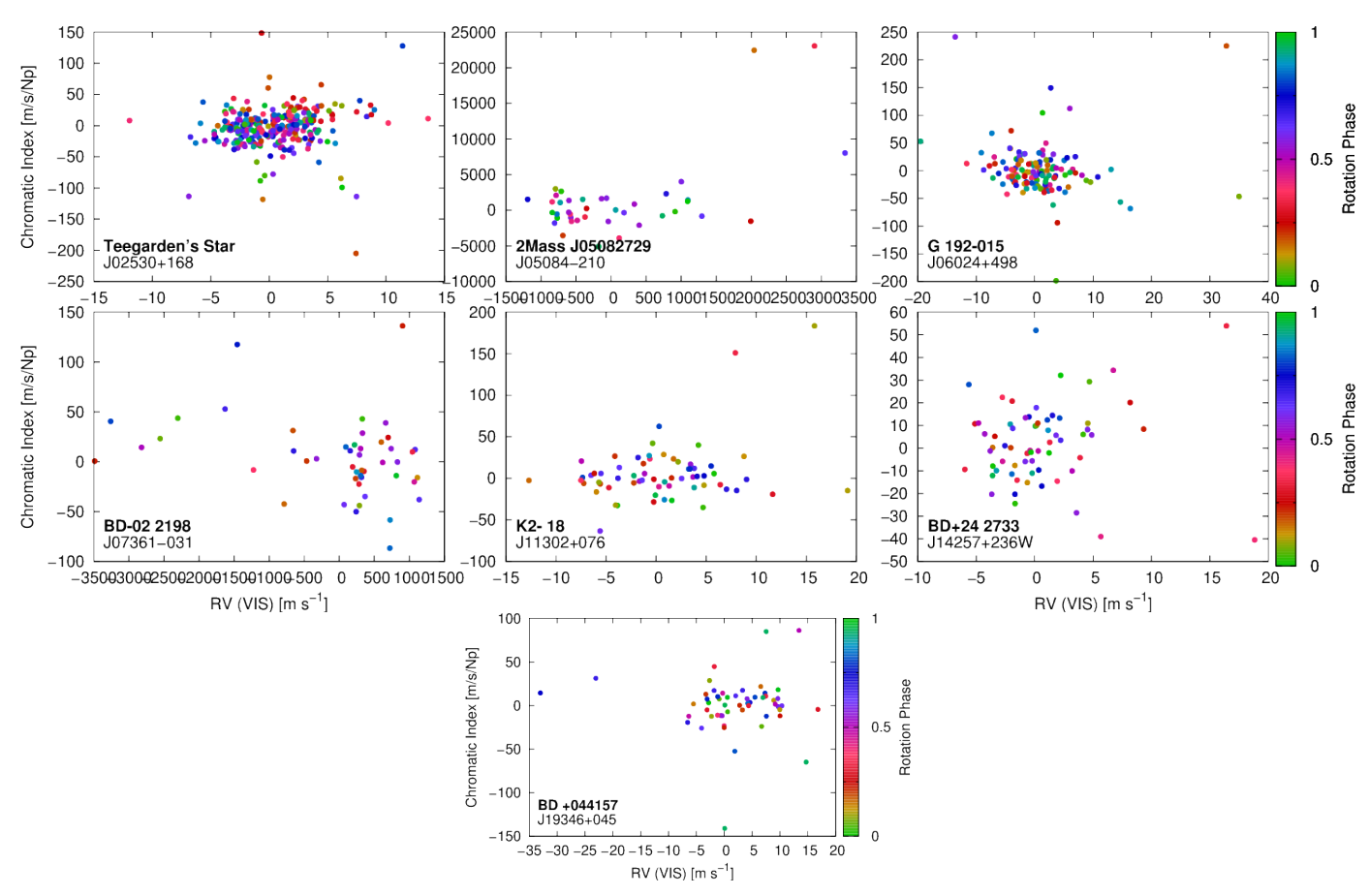


Fig. A.4. A selection of stars not showing a clear CRX slope. Their stellar parameters are shown in Table 4. Points are coloured by rotational phase derived from the rotation periods of Shan et al. (2024).

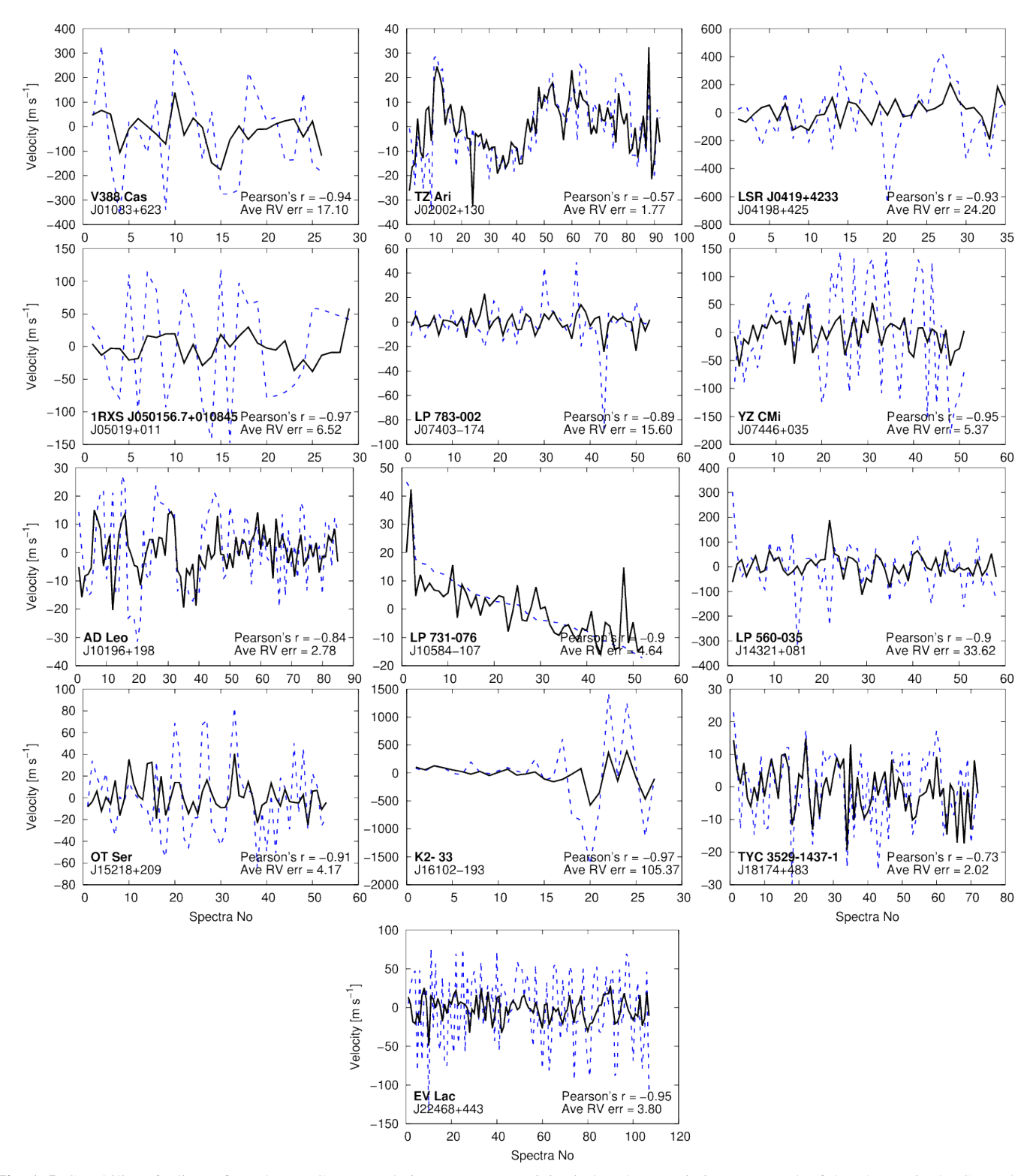


Fig. A.5. Capability of a linear fit to the RV-CRX correlation to remove activity-induced RV variations. For each of the 13 stars in the CRX-slope sample, the measured uncorrected RV for all CARMENES visible spectra is shown as a blue dashed line. The subtracted CRX values are shown as the solid black line. The rms values are shown in the key.

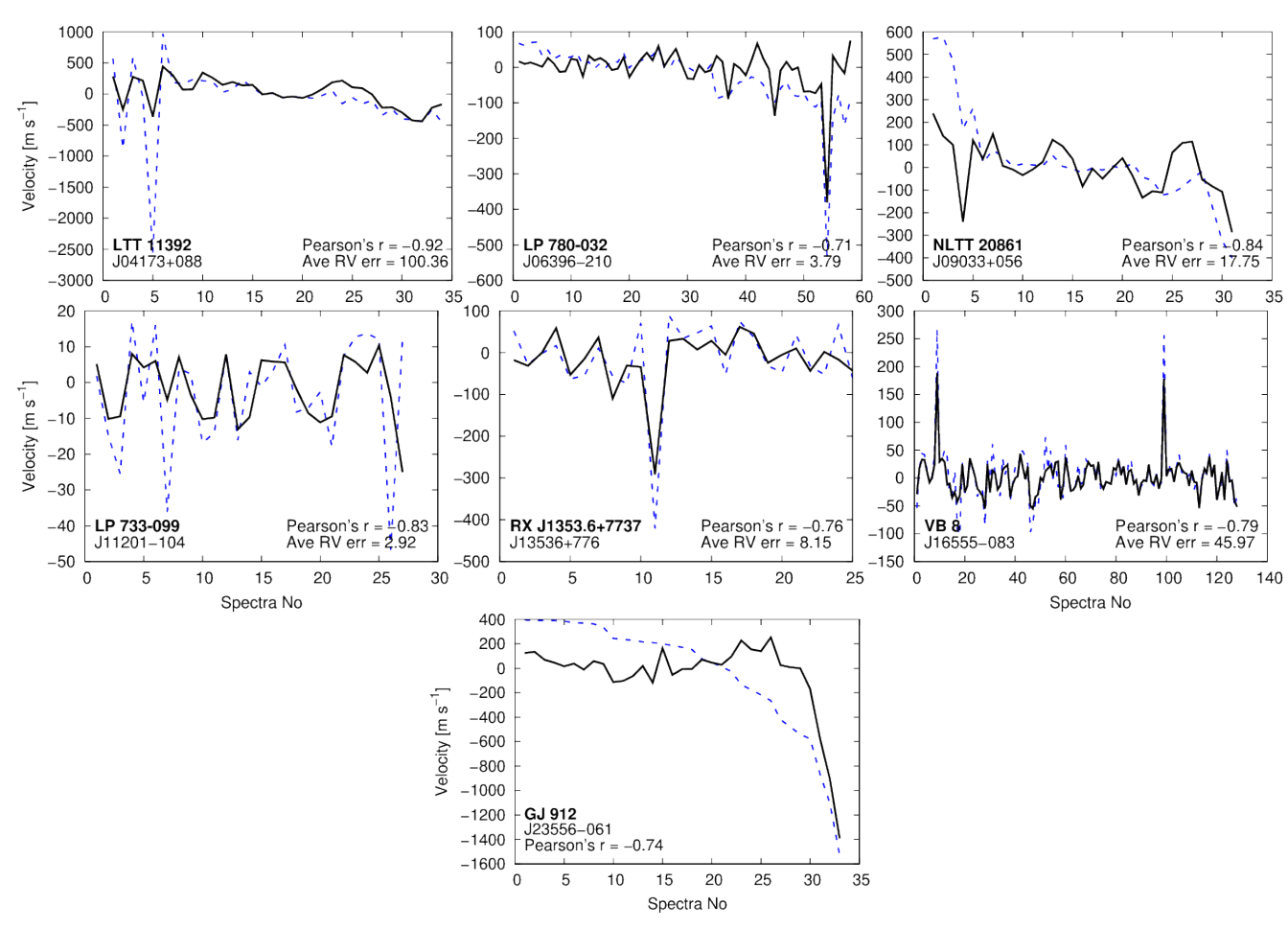


Fig. A.6. Same as Figure A.5 but for the Pearson sample with strong correlations only and factor of improvement values greater than 1.

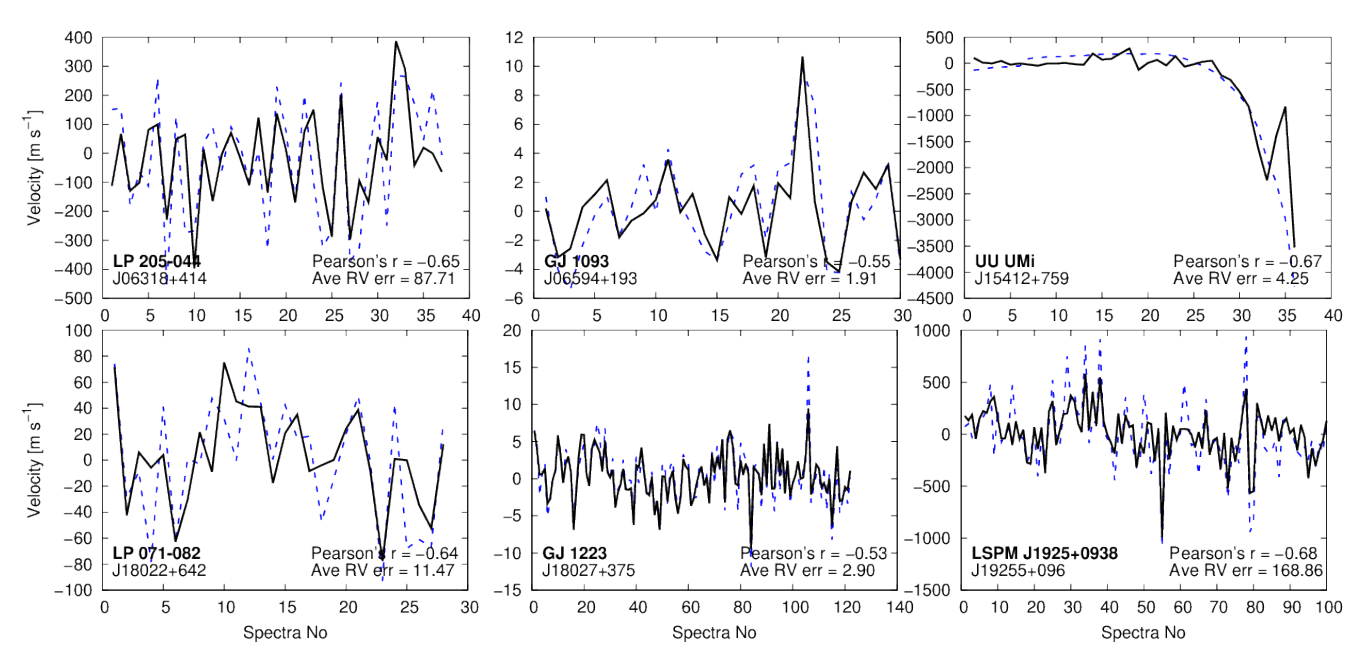


Fig. A.7. Same as Figure A.5 but for the Pearson sample with moderate correlations only and factor of improvement values greater than 1.

Appendix B: Stellar Parameters